Oda *et al. Earth, Planets and Space* (2022) 74:80
https://doi.org/10.1186/s40623-022-01626-1

Earth, Planets and Space

FULL PAPER Open Access

Matuyama–Brunhes geomagnetic reversal record and associated key tephra layers in Boso Peninsula: extraction of primary magnetization of geomagnetic fields from mixed magnetic minerals of depositional, diagenesis, and weathering processes

Hirokuni Oda[1*], Hiroomi Nakazato[2], Futoshi Nanayama[1] and Yumiko Harigane[1]

Abstract

We report paleomagnetic records of Matuyama–Brunhes geomagnetic polarity reversal and associated key tephra layers from the Early–Middle Pleistocene marine sedimentary succession in the Boso Peninsula. The outcrop is in Terasaki, Chiba, Japan and ~ 25 km northeast of the Chiba section. The sediment succession consists of a massive siltstone layer of the Kokumoto Formation, Kazusa Group. A tephra layer was identified in the middle of the outcrop with chemical composition comparable to that of the Byk-E tephra layer from the Chiba section defining the base of the Chibanian Stage. Oriented paleomagnetic samples were collected at intervals of 1–10 cm from the siltstone. To identify the primary remanent magnetization, progressive alternating field demagnetization (PAFD) and progressive thermal demagnetization (PThD) were conducted on pilot samples. Identification of primary magnetization with PAFD was not successful, especially for reversely magnetized samples. In addition, magnetization during PThD showed sharp drops around 175 °C, which decreased gradually between 175 °C and ~ 300 °C, and became unstable above ~ 350 °C. To extract the primary remanent magnetization while avoiding laboratory alteration by heating, a PThD up to 175 °C followed by PAFD was conducted. Combined analysis of remagnetization circles enables extraction of primary magnetization with improved reliability. Rock magnetic experiments were conducted during stepwise heating to understand the magnetic minerals involved and to evaluate the influence of laboratory heating. During heating, FORC-PCA revealed significant changes of magnetic minerals at 200 °C, 400 °C, 450 °C and 550 °C. Rock magnetic analyses and electron microscopy indicate that titanomagnetite/magnetite are magnetic minerals contributing to primary remanent magnetization. Greigite was also identified preserving secondary magnetizations during sub-seafloor diagenesis. The presence of feroxyhyte is suggested as secondary magnetization through the weathering of pyrite by exposure to the air after the Boso Peninsula uplift. The correlation of relative paleointensity with the Chiba section provides an age model with sedimentation rates of 30 cm/kyr and 18 cm/kr for the intervals above and below the Byk-E tephra. VGP

*Correspondence: hirokuni-oda@aist.go.jp

[1] Research Institute of Geology and Geoinformation, Geological Survey of Japan, AIST, Central 7, 1-1-1 Higashi, Tsukuba 305-8567, Japan
Full list of author information is available at the end of the article

latitudes are highly consistent with those from the Chiba section based on the age model, which assigns the main directional swing from reversed to normal polarities as 772.8 ± 0.5 ka.

Keywords: Paleomagnetism, Magnetostratigraphy, Matuyama–Brunhes polarity transition, Boso Peninsula, Magnetite, Greigite, Diagenesis, Pyrite, Remagnetization circle, Primary remanent magnetization

Graphical Abstract

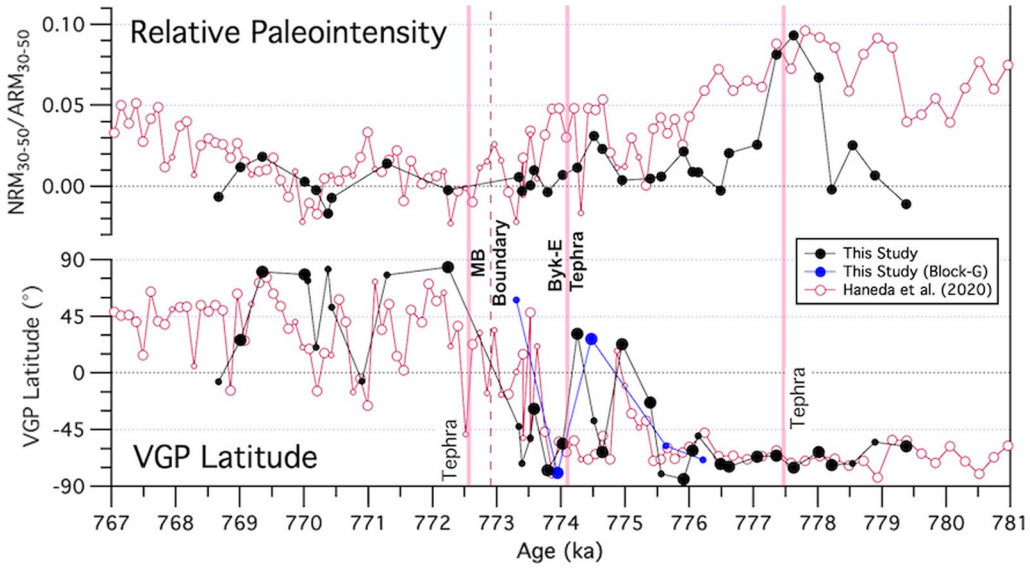

Introduction

The Matuyama–Brunhes (M–B) boundary, the Earth's latest geomagnetic field reversal event, is an important calibration point on the geological timescale, providing a clear marker in the Pleistocene, which has been the focus of many paleomagnetic studies. Studies have been conducted on the M–B boundary using sediments (Clement and Kent 1991; Oda et al. 2000; Channell and Kleiven 2000; Channell et al. 2010) and volcanic rocks (Mochizuki et al. 2011; Ricci et al. 2020), both of which have advantages and complement each other. During the polarity transition, the Earth's geomagnetic field intensity dropped significantly (Valet et al. 2005; Valet and Fournier 2016). In addition, the reduction in geomagnetic field intensity has been recorded as increased production of cosmogenic radionuclides in the upper atmosphere, including ^{10}Be in marine sediments (Suganuma et al. 2010; Valet et al. 2014) and in an Antarctic ice core (Raisbeck et al. 2006; Dreyfus et al. 2008).

The geomagnetic field intensity data as well as directional records during polarity transitions contain essential information about the Earth's core and its boundary conditions, which are expected to lead to geodynamic models that can explain geomagnetic reversals (e.g., Merrill and McFadden 1999; Leonhardt and Fabian 2007; Nakagawa 2020; Tassin et al. 2021). In particular, preferred paths of transitional virtual geomagnetic poles (VGPs) are considered to hold invaluable information on the conditions at the core–mantle boundary, which have been made evident during the transitions (Clement 1991; Laj et al. 1991; Hoffman and Mochizuki 2012; Hoffman et al. 2020). Importantly, the reversal process is rapid but dynamic compared with the normal process of geomagnetism. Thus, retrieving continuous paleomagnetic records of adequate temporal resolution from sediments could allow us to accumulate the information necessary to understand the reversal process.

In the Boso Peninsula, thick Pleistocene marine sediments, the Kazusa Group and the overlying Shimosa Group were deposited (Additional file 1: Figure S1). The Kazusa Group is well exposed and contains a continuous stratigraphic succession with well-preserved marine microfossils, pollen, paleomagnetic reversal events, and many tephra layers (Kazaoka et al. 2015; Haneda et al. 2020; Nishida et al. 2016; Okada et al. 2017; Suganuma et al. 2018, 2021). The M–B boundary is widely distributed in the area (e.g., Okada and Niitsuma 1989; Kazaoka et al. 2015; Hyodo et al. 2016). The high rate of sedimentation with numerous tephra layers allowed high-resolution magnetostratigraphy studies on the Boso Peninsula.

In 2020, the Executive Committee of the International Union of Geological Sciences ratified the Global Boundary Stratotype Section and Point (GSSP), defining the base of the Chibanian Stage in the Chiba section, Japan (Additional file 1: Figure S1; Suganuma et al. 2021). The sediments captured both terrestrial and marine environmental signals, as well as the last geomagnetic field reversal. The Chiba section reveals a tightly defined Matuyama–Brunhes paleomagnetic polarity boundary, geomagnetic field paleointensity proxies, and numerous tephra beds, allowing the establishment of a robust and precise chronostratigraphic framework.

The M–B boundary was identified in the middle part of the Kokumoto Formation of the Kazusa Group in the central Boso Peninsula by Nakagawa et al. (1969) and Niitsuma (1971, 1976). A series of paleomagnetic studies identified the M–B boundary approximately 2 m below the Ontake-Byakubi-E (Byk-E) tephra bed using alternating field (AF) demagnetization (Niitsuma 1971; Okada and Niitsuma 1989; Tsunakawa et al. 1995, 1999). In contrast, recent paleomagnetic records using thermal demagnetization by Suganuma et al. (2015), Okada et al. (2017), and Haneda et al. (2020) for the Chiba section indicate that the M–B boundary is located slightly above the Byk-E tephra bed, which provides magnetostratigraphic bases for the proposal and the final ratification of the GSSP.

The age of 780 ka for the M–B boundary, which has been frequently cited in the literature, was derived from astronomically tuned benthic and planktonic oxygen isotope records from the eastern equatorial Pacific (Shackleton et al. 1990). This astronomical age of the M–B boundary is supported by the $^{40}Ar/^{39}Ar$ ages of 775.6 ± 1.9 ka obtained from lavas recording the reversal in Hawaii (Coe et al. 2004; Singer et al. 2005), which has been updated to 781–783 ka based on the revised age of the Fish Canyon Tuff sanidine standards (Kuiper et al. 2008; Renne et al. 2011). Furthermore, it has been shown that the lock-in of the geomagnetic signal occurs below the sediment–water interface in marine sediments (e.g., Roberts et al. 2013; Suganuma et al. 2011), which means a delayed magnetization acquisition yielding older ages for geomagnetic events than the actual depositions. Assuming a constant lock-in depth for a delayed magnetization acquisition, higher rates of sedimentation should minimize the age offset for geomagnetic field events (deMenocal et al. 1990; Suganuma et al. 2010). This is evidenced by the fact that the youngest astrochronological M–B boundary ages of 772–773 ka were reported for high sedimentation rate records (Channell et al. 2010; Valet et al. 2014). These M–B boundary ages are consistent with the records of cosmogenic nuclides in marine sediments (Suganuma et al. 2010; Simon et al. 2016, 2018) and an Antarctic ice core (Raisbeck et al. 2006; Dreyfus et al. 2008), which are free from magnetization lock-in.

Suganuma et al. (2015) reported a U–Pb zircon age of 772.7 ± 7.2 ka for the Byk-E tephra bed. The Byk-E tephra is 1.1 m below the directional midpoint in the Chiba section, where the GSSP is positioned at the base. Astronomical calibration using oxygen isotope records further pinned down the age of the Byk-E tephra to 774.1 ka, which is immediately below the top of Marine Isotope Substage 19c (Suganuma et al. 2021). On the other hand, the M–B boundary in the Chiba section has an astronomically estimated age of 772.9 ka (Suganuma et al. 2018), which is consistent with astronomically tuned paleomagnetic records (Channell et al. 2010; Channell 2017; Valet et al. 2019), and cosmogenic nuclide records (Raisbeck et al. 2006; Suganuma et al. 2010; Simon et al. 2018; Valet et al. 2019).

After the application of simple thermal demagnetization by Suganuma et al. (2015), improvements were made by Okada et al. (2017) to extract primary remanent magnetizations from weakly magnetized sediments influenced by diagenesis using thermal demagnetization (ThD) up to 300 °C, followed by AF demagnetization (AFD). Haneda et al. (2020) followed the procedure of Okada et al. (2017) and provided high-quality paleomagnetic data, which finalized paleomagnetic evidence for the GSSP. Here, we report paleomagnetic records with geomagnetic reversals corresponding to the M–B boundary from silty clay sediments recovered from an outcrop around Terasaki in the Boso Peninsula (Nanayama et al. 2016). Three tephra layers have been identified in the studied outcrop, and the middle one could be correlated with the Byk-E tephra bed, a stratigraphic marker defined as the base of Chibanian (Suganuma et al. 2021). We also demonstrate the applicability of ThD followed by AFD on mixed polarity intervals with unstable magnetization affected by diagenesis, which is comparable to the records for the GSSP reported by Haneda et al. (2020). Further, we show the details of the magnetic minerals involved and evaluate the influence of laboratory heating on magnetic minerals. Finally, we investigated the secondary magnetization carried by iron sulfide minerals associated with sub-seafloor diagenesis and iron oxides generated by iron sulfide oxidation during weathering after uplifting of Boso Peninsula sediments.

Geological background, samples and methods

Geological background

Thick marine sediments were deposited around the Japanese Islands in response to the subduction of the Pacific Plate beneath the Philippine Sea and North American plates during the Pleistocene (Additional file 1:

Figure S1). In the Boso Peninsula, deep- and shallow-water marine succession of ~ 3,000 m thick, the Kazusa Group, was deposited in the early and middle Pleistocene (Additional file 2: Figure S2a). Based on calcareous nannofossils (Sato et al. 1988), planktonic foraminifera (Oda 1977), diatoms (Cherepanova et al. 2002), magnetostratigraphy (Niitsuma 1976), and oxygen isotope stratigraphy (Okada and Niitsuma 1989; Pickering et al. 1999; Tsuji et al. 2005), depositional ages were estimated as ca. 2.4 to 0.5 Ma for the Kazusa Group (Ito, 1992; Ito et al. 2016). In addition, a number of tephra beds provide detailed stratigraphic correlations and the compilation of different types of age data (Machida et al. 1980; Satoguchi and Nagahashi, 2012). These tephras from the Kazusa Group were dated using zircon fission-track dating (Tokuhashi et al. 1983; Kasuya, 1990; Watanabe and Danhara, 1996; Suzuki et al. 1998), U–Pb dating using SIMS (Suganuma et al. 2015), and LA-ICP-MS (Ito et al. 2017). The Byk-E tephra bed, originating from the Older Ontake volcano in Central Japan (Takeshita et al. 2016), was defined as the base of the Chibanian Stage/Age (Suganuma et al. 2021). The Kazusa Group is subdivided into 12 formations (Additional file 2: Figure S2a): the Kurotaki, Katsuura, Namihana, Ohara, Kiwada, Otadai, Umegase, Kokumoto, Kakinokidai, Chonan, Kasamori, and Kongochi Formations in stratigraphic ascending order (Kazaoka et al. 2015).

Samples

Paleomagnetic samples were taken from an outcrop located within the area of the Geological Map of Mobara (Nanayama et al. 2016), which is dominated by siltstones exposed in Terasaki Shinden-Nishi along a roadside in the Mobara district, Chiba Prefecture, Japan (Lat. = 35.381058°N, Lon. = 140.311016°E; Additional file 1: Figure S1). The outcrop is ~ 4 m in height, facing west with a tilt angle of ~ 52° (Additional file 3: Figure S3). The lithology of the outcrop is mainly massive siltstone of the Kokumoto Formation (Additional file 2: Figure S2b), Kazusa Group. The outcrop contains three tephra layers A, B and C. The very fine sand to silt-sized tephra B layer (0–3 mm thick) is located in the middle of the outcrop, which is presumed to be the Byk-E layer and should be slightly below the M–B boundary (Suganuma et al. 2015, 2018; Okada et al. 2017; Simon et al. 2019; Haneda et al. 2020). In addition, the pumiceous tephra A and C layers (both are 2–3 cm thick) are located 47 cm above and 60 cm below of tephra B, respectively. The dips of thin sand layers within the thick siltstone are less than ten degrees. Thus, we consider the bedding plane of the strata for the studied outcrop is subhorizontal; no tilt correction on the paleomagnetic results. To identify the paleomagnetic polarity for magnetostratigraphy, we collected oriented paleomagnetic drill cores (1-in. diameter) at intervals of 1–10 cm from 7 blocks (A-G, Additional file 3: Figure S3(c)) in the outcrop (Additional file 4: Figure S4; Additional file 6: Table S1a). Tephra layer B is in the middle between paleomagnetic samples 60 (1.2 cm below of tephra B) and 61 (1.2 cm above of tephra B). Paleomagnetic samples 76 (49.3 cm above of tephra B) and 30 (57.9 cm below of tephra B) are located several centimeters from the base of tephra layers A and C, respectively. Tephra layers, particularly for tephra B, were also collected for chemical analyses.

Tephra analyses

Chemical analyses were performed to confirm that tephra B is correspondent to the Byk-E layer. Since no glass shards were recognized after washing, hornblende grains were picked up from tephra B and analyzed for chemical compositions and compared with those for Byk-E from the Chiba section. Volcanic glass shards taken from a tephra layer, corresponding to the Byk-E, ~ 7 km west of the Terasaki section (M44 in the map of Nanayama et al. 2016; Additional file 1: Figure S1b) were also analyzed and compared with those from the Byk-E in the Chiba section. For chemical analyses, the following two types of scanning electron microscope (SEM) were used (Table 1): (a) energy dispersive X-ray spectroscopy (EDS; HORIBA EX-270) in a SEM (HITACHI SU1510), and (b) EDS (HORIBA EX-250) in a SEM (HITACHI S3000H), with an acceleration voltage of 15 kV, an electric current of 0.3 nA, and a beam diameter of 150 nm at the Furusawa Geological Survey, Japan.

Scanning electron microscope analyses

Highly polished thin sections of samples 77A and 83A were prepared for scanning electron microscope analyses. Observations and mineral identification in the thin sections were carried out using a SEM (HITACHI SU3500) equipped with EDS ($Xmax^{80}$ in Oxford Instruments) and electron back-scattered diffraction (EBSD; HKL NordlysNano in Oxford Instruments) at GSJ-Lab. These measurements were performed using the Aztec software (Oxford Instruments). EBSD measurements were conducted under an accelerating voltage of 15 kV, working distance of 18–22 mm, specimen tilting to 70°, and low-vacuum mode. All index data represent points with a mean angular deviation of $\leq 1°$. The EDS analysis was also conducted under an acceleration voltage of 15 kV, a working distance of 10 mm, and the high-vacuum mode.

Paleomagnetic and rock magnetic measurements

Two or three specimens (1.1 or 2.2 cm in length) were obtained from each drill core and subjected to

Table 1 Chemical analysis of a tephra layer (tephra B) from Terasaki section (this study), Byk-E from Yoro river (the Chiba section) and Byk-E from M44 section (Nanayama et al. 2016)

Target	Tephra	N	Method		Oxides (wt%)									
	Loc				SiO2	TiO_2	Al_2O_3	FeO	MnO	MgO	CaO	Na_2O	K_2O	Total
Hornblende	Byk-E	20	a	Average	44.25	1.84	10.15	13.16	0.78	13.52	10.67	1.92	0.49	96.78
	Yoro River			Std. Dev	0.99	0.31	0.94	0.61	0.29	0.61	0.30	0.16	0.05	0.43
	Tephra B	5	a	Average	45.07	1.75	9.29	13.13	0.33	13.73	10.89	1.73	0.36	96.29
	Terasaki			Std. Dev	2.99	0.58	2.81	2.54	0.16	1.50	0.45	0.42	0.18	0.52
Volcanic glass	Byk-E	20	b	Average	66.76	0.21	12.97	1.14	0.13	0.26	1.74	3.51	2.92	89.63
	Yoro River			Std. Dev	0.79	0.07	0.59	0.12	0.06	0.05	0.31	0.20	0.20	0.84
	Byk-E	20	a	Average	67.00	0.21	12.79	1.23	0.16	0.31	1.67	3.49	2.93	89.79
	M44			Std. Dev	0.80	0.05	0.16	0.12	0.08	0.04	0.07	0.07	0.07	1.00
N: number of measured grains														
Method	a	EDS: HORIBA EMAX Evolution EX-270, SEM: HITACHI SU1510, acceleration voltage of 15 kV and a beam current of 0.3nA												
	b	EDS: HORIBA EMAX ENERGY EX-250, SEM: HITACHI S3000H, acceleration voltage of 15 kV and a beam current of 0.3nA												

progressive demagnetization experiments. To identify the primary remanent magnetization and for subsequent stratigraphic correlation, the following processes were conducted at GSJ-Lab, AIST. Low-field magnetic susceptibility was measured for all specimens using a Kappabridge susceptibility meter (KLY-4S; AGICO). Subsequently, the natural remanent magnetization (NRM) was measured using a three-axis cryogenic magnetometer (SRM-760R; 2G Enterprises) in a magnetically shielded room. For each drill core or for each sampling horizon from block G, a specimen was selected to perform progressive alternating field demagnetization (PAFD) at 1–10 mT increments up to 80 mT using an AF demagnetizer in line with the magnetometer. Several pilot specimens for progressive thermal demagnetization (PThD) were selected and then heated in air at 25–50 °C increments up to 500 °C using a thermal demagnetizer (TDS-1; Natsuhara-Giken). For the specimens other than the pilot ones, PThD in vacuum up to 175 °C followed by AF demagnetization up to 80 mT was conducted. For this process, low-temperature demagnetization with liquid nitrogen (e.g., Ozima et al. 1964) was conducted before each AF demagnetization step to minimize the influence of multidomain magnetization. When three specimens from each core were available, ThD in air up to 300 °C and subsequent PAFD up to 80 mT were conducted. For specimens from block G collected during the second sampling, PThD in air up to 175 °C followed by PAFD up to 80 mT was conducted. We also applied other complex combined demagnetization methods on specimens from block G for the purpose of minimizing laboratory alteration by heating while maximizing the extraction of primary remanent magnetization. The details on the methods, and motivations, advantages and disadvantages are shown in Additional file 6: Table S1b. Paleomagnetic data were processed using Paleomagnetism.org 2.0 (Koymans et al. 2016, 2020) including features on combined analyses of remagnetization circles (McFadden and McElhinny 1988).

Several rock magnetic experiments were conducted on the studied specimens to identify their magnetic mineral components. Thermal demagnetization of the three-component IRM (isothermal remanent magnetization) was performed on selected specimens based on Lowrie (1990). For each specimen, IRM was imparted with a magnetic field of 2.5 T in the Z-axis using a pulse magnetizer (Model 660; 2G Enterprises) at GSJ-Lab, AIST. A secondary IRM was put at 0.4 T in the Y-axis, which was followed by a field of 0.12 T applied in the X-axis. The procedure makes each specimen acquire magnetization for high (0.4–2.5 T), medium (0.12–0.4 T), and low (0–0.12 T) coercivity components in the Z, Y, and X axes, respectively. The specimens were thermally demagnetized stepwise to monitor the unblocking temperatures of different coercivities and deduce possible magnetic mineral components in the specimens.

Chips of selected specimens were weighted and their magnetic hysteresis parameters (M_s, M_{rs}, B_c, and B_{cr}) were measured using an alternating gradient magnetometer (PMC MicroMag 2900 AGM; Lake Shore Cryotronics Inc.) or vibrating sample magnetometer (Model 8604 VSM; Lake Shore Cryotronics Inc.) at GSJ, AIST. The ratio of saturation remanent magnetization to saturation magnetization (M_{rs}/M_s) was plotted versus the ratio of coercivity of remanence to coercivity (B_c/B_{cr}) based on the method proposed by Day et al. (1977). In addition, measurements of the first-order reversal curve (FORC) were performed, which provide enhanced mineral

and domain state discrimination (Roberts et al. 2014). FORC results were processed using FORCinel (Harrison and Feinberg 2008), and principal component analysis (FORC-PCA) was conducted (Lascu et al. 2015; Harrison et al. 2018). Low-temperature magnetic properties were measured on a sample chip using a magnetic property measurement system (MPMS-5XL; Quantum Design Inc.) at GSJ. The magnetic moment was monitored during warming in a 4-mT field following a zero-field cooling, which provides information on the magnetic transition temperatures of magnetic minerals (e.g., Verwey transition for magnetite (Verwey 1939) and Morin transition for hematite (Morin 1950)).

Results

Tephra analyses

Table 1 summarizes the chemical compositions of the tephra layers from the Terasaki section and nearby sections (the Chiba section and M44). Hornblendes from tephra B of Terasaki section (this study) show similar compositions with those from Byk-E of the Chiba section, suggesting that the tephra B corresponds to Byk-E (with an astronomically calibrated age of 774.1 ka; Suganuma et al. 2021). To evaluate the similarity objectively, the similarity coefficient (SC) value was calculated for the elements of the two tephras, considering analytical errors based on Eq. (2) by Borchardt et al. (1971). The lower bound of the SC value for the acceptance of correlation is 0.92 (Froggatt 1992). The SC values calculated from the analytical results of tephra B and Byk-E were 0.96, suggesting that these two tephras are correlated. The volcanic glasses for Byk-E of M44 and the Chiba section provided an SC value of 0.97, which confirms the same origin.

Scanning electron microscope analyses

Figure 1 shows the results of electron microscopy analyses for iron oxide and sulfide minerals in sample 77A. The upper mineral with bright reflection in the back-scatter electron image (Fig. 1a) is composed of Fe (Fig. 1c), Ti (Fig. 1d), and O (Fig. 1e). EBSD analysis for point A of the mineral shows a clear Kikuchi pattern indicative of titanomagnetite (Fig. 1f and g). The morphology of titanomagnetite grains is angular (Fig. 1a). Based on their morphology, these grains are considered to be of detrital or volcanic origin and were transported from the Japanese Islands. Lower minerals with bright reflections and framboidal textures (Fig. 1a) are composed of S (Fig. 1b) and Fe (Fig. 1c) in the central part, whereas the outer part of the framboid is composed of Fe (Fig. 1c) and O (Fig. 1d). EBSD analysis for point B of the framboid shows a Kikuchi pattern indicative of pyrite (Fig. 1h and i). Outer part of the framboid composed of Fe and O is considered to be an indication of oxidative weathering of pyrite.

Framboidal sulfide minerals are ubiquitous and are typically observed as dense fillings in the chambers of microfossil shells, such as foraminifera in sample 83A (Fig. 2a). Figure 2b is a close-up image of an area in Fig. 2a. Sulfide minerals were composed of coarse (~1 μm) and fine (~0.3 μm) grained mineral assemblages and their morphologies suggest that they are originated from diagenesis. Figure 2c and d shows the EDS spectra of point A (coarse grain) and B (fine grain) with characteristic peaks of Fe and S, respectively. The peaks for S are lower in Fig. 2d than in c, indicating a lower atomic ratio of S in the grain for Point B than that for Point A.

The microstructure of these sulfide minerals closely resembles to those reported by Roberts et al. (2011) in their Fig. 2e with coarse grains (~1 μm; interpreted as pyrite) and fine grains (~0.3 μm; interpreted as greigite). EBSD analysis of coarse grains shows Kikuchi patterns indicative of pyrite, supporting this interpretation. Although EBSD for fine grains was not successful, the EDS of a fine grain showed a subdued peak of sulfur (Fig. 2d) compared with that of a coarse grain (Fig. 2c) relative to the peak of iron, which also suggests that the fine-grained framboids are greigite. Although the presence of fine-grained greigite is suggested in the range of SD (~0.3 μm; e.g., Roberts et al. 2011), possible presence of MD greigite cannot be excluded.

Paleomagnetism

PAFD was conducted on the specimens from each drill core sample. Typical behaviors against PAFD are shown in Fig. 3b and e, indicating the removal of viscous overprint by AF demagnetization up to 2–10 mT. The higher coercivity (> ~20 mT) magnetization component shows a mostly positive inclination for sample 77 around the stratigraphic level +57 cm (normal polarity; Fig. 3e), whereas sample 27 around the stratigraphic level of −63 cm show negative inclination (reversed polarity; Fig. 3b). On the other hand, typical PThD in air shows a significant drop in NRM upon heating from 100 °C to 175 °C as shown from sample 2 at the stratigraphic level −116 cm (Fig. 3a and its inset). Upon heating above

(See figure on next page.)

Fig. 1 SEM analyses of iron oxide and sulfide minerals. **a** Back scatter electron image taken from a thin section of Sample 77A. **b** S, **c** Fe, **d** T, and **e** O images obtained by EDS analysis within the area shown by a red rectangle in **a**. **f** Kikuchi pattern obtained for point A in **a** by EBSD analysis, and **g** those with best interpreted Kikuchi bands (pink lines), their midlines (yellow broken lines) and index numbers (digits) for titanomagnetite. **h** Kikuchi pattern obtained for point B in **a**, and **i** those with best interpretations for pyrite

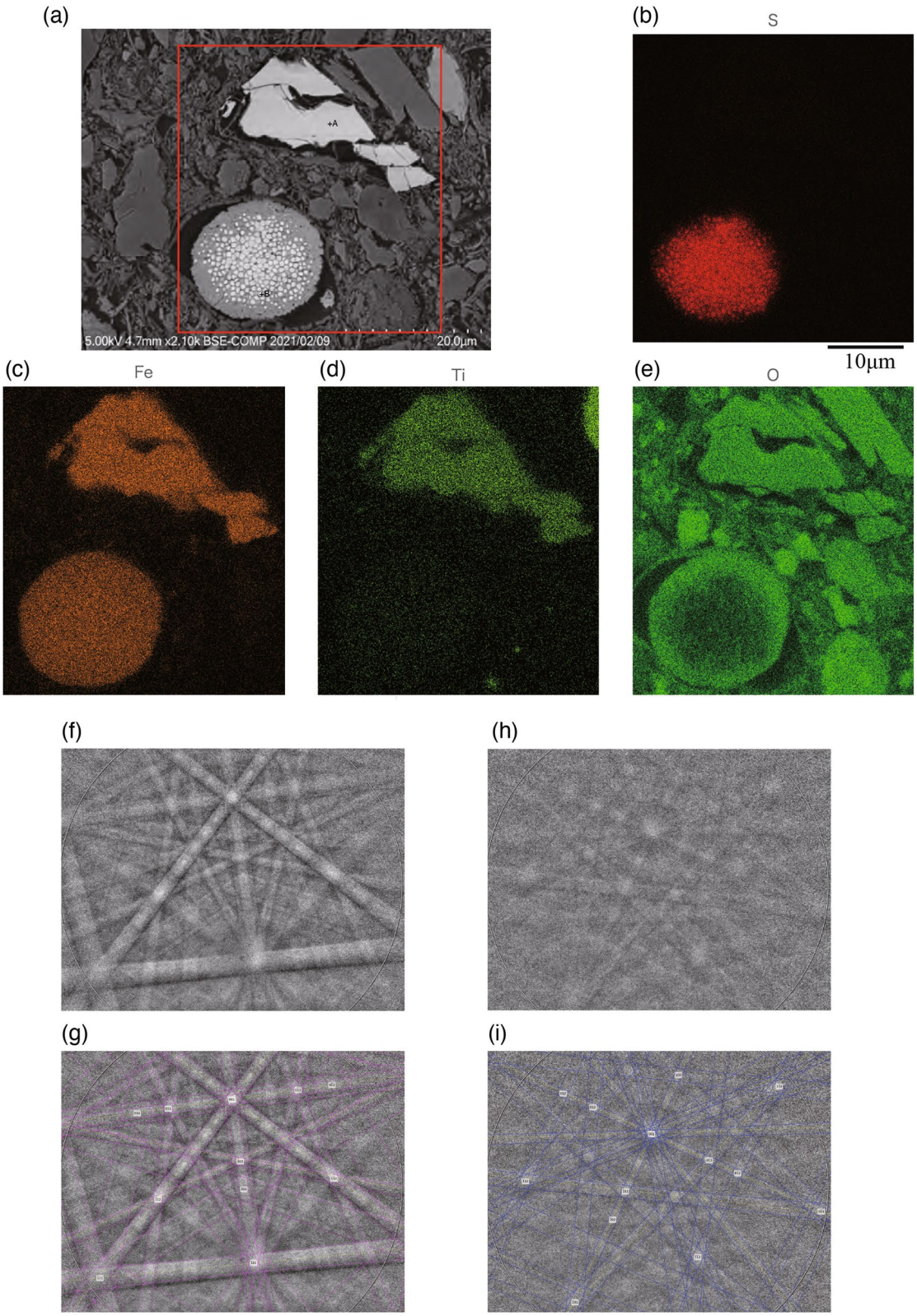

Fig. 1 (See legend on previous page.)

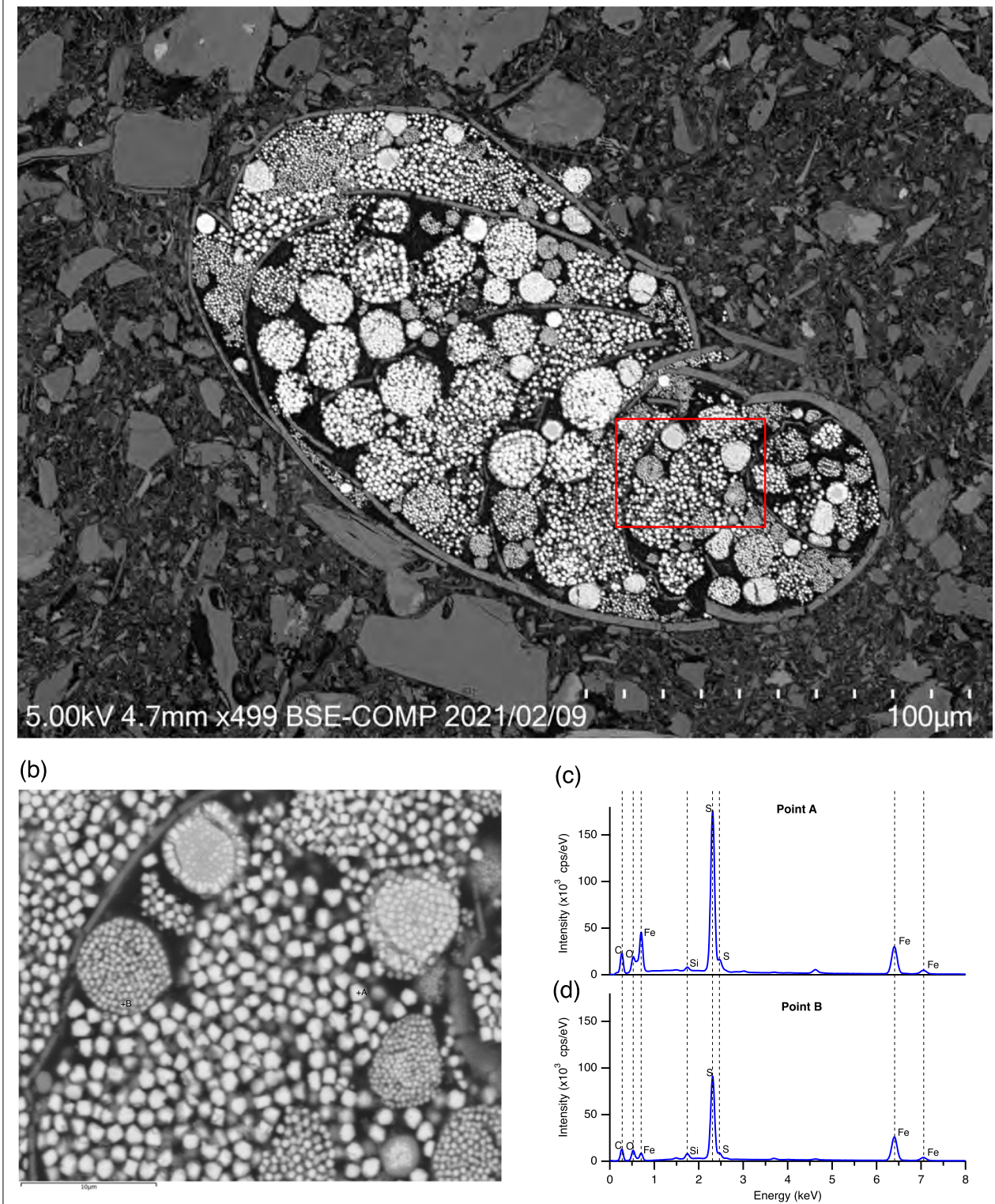

Fig. 2 SEM analyses on framboidal sulfides. **a** Back scatter electron image taken for a thin section from Sample 83A. Framboidal sulfide minerals are densely filling the chambers of foraminiferal shell. **b** Close up of the area in **a** shown by a red rectangle. Framboidal sulfide minerals were composed by coarse (~ 1 micro-m) and fine (~ 0.3 micro-m) grain-size. **c** and **d** are spectrum of point A (coarse grain) and B (fine grain) with characteristic peaks of Fe and S, respectively

175 °C, the magnetization decreases gradually up to 300–350 °C (Fig. 3a) and becomes unstable above ~ 350 °C. Considering the significant drop of NRM by heating up to 175 °C without instability, we conducted PAFD following PThD up to 175 °C in vacuum (Fig. 3d and f). Although not all specimens exhibit ideal behavior decaying linearly toward the origin, some samples show satisfactory results indicative of primary magnetization (e.g., Fig. 3d and f). In addition, some specimens were conducted with PAFD following PThD up to 300 °C in air; Fig. 3c shows one of the specimens exhibiting successful results with negative inclination decaying linearly to the origin.

Figure 4 shows the plots of the volume magnetic susceptibility and paleomagnetic results versus depth, where a horizontal broken line at zero indicates the position of the Byk-E tephra. The horizontal lines above and below the Byk-E tephra are tephra A and tephra C, respectively. The two samples slightly above tephra A (sample 76) and tephra C (sample 30) show peaks in susceptibility (Fig. 4a) and NRM intensity (blue solid circles, Fig. 4b), suggesting that these samples contain volcanic materials.

The NRM intensity before demagnetization were significantly reduced after AFD at 30 mT (blue open diamonds, Fig. 4b). PAFD at 30 mT for samples 24, 27 and 30 with stratigraphic levels between −70 and −60 cm show declinations around 180°, and negative or low positive inclinations (Fig. 4c and d). Susceptibility and NRM after AFD at 30 mT for this interval (Fig. 4a and b) show much higher values than the other stratigraphic intervals. This suggests that these samples acquired more stable primary magnetization during a reversed polarity interval that could be resolved using only AFD, whose behaviors against demagnetizations are different from the other intervals. On the other hand, the paleomagnetic directions obtained by the linear regression fitting for the PAFD experiments after heating in air or in vacuum suggest that the samples with stratigraphic levels from −90 to +20 cm have negative inclination for most of the interval (Fig. 4f). Since thermal demagnetizations were conducted on specimen B for samples 1 ~ 10 as pilot studies, which resulted in instability above 350 °C, no specimens were left for the PAFD experiments following heating. Also, demagnetization behavior against heating between 200 °C and 350 °C are not reliable enough, based on the interpretations using combined demagnetization methods and remagnetization circles on other samples. To avoid misinterpretation, we decided not to use these samples from stratigraphic levels between −120 and −100 cm for the interpretation of paleomagnetic directions (Fig. 4e and f; Additional file 7: Table S2). The paleomagnetic directions of the linear regression fitting for the PAFD experiments after heating in air or in vacuum for intervals above + 20 cm has mostly positive inclinations except samples 76 (~ 49 cm), 87(~ 119 cm), and 93 (164 cm) (Fig. 4f; Tables S2). Despite this, the results of linear regression fitting on PAFD experiments after partial heating to 175 °C (in air and vacuum) and 300 °C (in air) are not always satisfactory, with large MAD values (> 15°), and transitional behavior of paleomagnetic directions. Further investigation will be conducted in the following subsection 'combined analyses of remagnetization circles'.

Rock magnetism

Figure 5 shows the results of the low-temperature magnetic property measurements of a sediment sample with the MPMS. Magnetization during warming in the 4 mT field shows a clear inflection point at ~ 117 K. This could be considered as a magnetic transition temperature representative of magnetite (Verwey transition; Verwey 1939). The transition temperature close to that of stoichiometric magnetite (~ 125 K) may suggest the presence of nearly pure magnetite (or low-Ti magnetite based on EDS analysis, Fig. 1d) grains in the sample. A subdued signal of the transition may indicate a partial oxidation (e.g., Ozdemir et al. 1993).

Figure 6 is a typical example of the results of the thermal demagnetization experiments of the three-axis IRM. The low coercivity component (0–0.12 T) shows a significant decrease in intensity at approximately 480–560 °C. The low coercivity component also shows a broad decrease around 200–400 °C. The medium coercivity component (0.12–0.4 T) shows a significant decrease of IRM at temperatures around 200–300 °C. The high coercivity component (0.4–2.5 T) is not significant and shows a gradual decrease during heating up to 600 °C. Magnetic susceptibility shows an increase from 400 to 440 °C, which may indicate the production of magnetic

(See figure on next page.)

Fig. 3 Typical Zijderveld diagrams for sample 2 (**a**), sample 27 (**b**, **c**, and **d**) and sample 77 (**e** and **f**). Samples 2, 27, and 77 correspond to stratigraphic levels of −116 cm, −63 cm, and +57 cm relative to the Byk-E tephra layer, respectively. **a** PThD for specimen 2B up to 500 °C. Inset is a plot showing magnetization versus temperature. **b** PAFD for specimen 27A-1. **c** PThD for specimen 27B up to 300 °C (left) followed by PAFD (right). **d** PThD for specimen 27A-2 up to 175 °C (left), and subsequent PAFD following LTD at each step (right). **e** PAFD for specimen 77A-1. **f** PThD for specimen 77A-2 up to 175 °C (left), and subsequent PAFD following LTD at each step (right). Sample 27 (**b**, **c**, and **d**) and sample 77 (**e** and **f**) are considered to have reversed and normal polarity of primary remanent magnetizations, respectively. Stratigraphic distance of paleomagnetic samples from Byk-E are after correction of slope of the outcrop. For each specimen, stratigraphic distance from Byk-E (Additional file 6: Table S1a) is shown after correction of slope of the outcrop in the parentheses

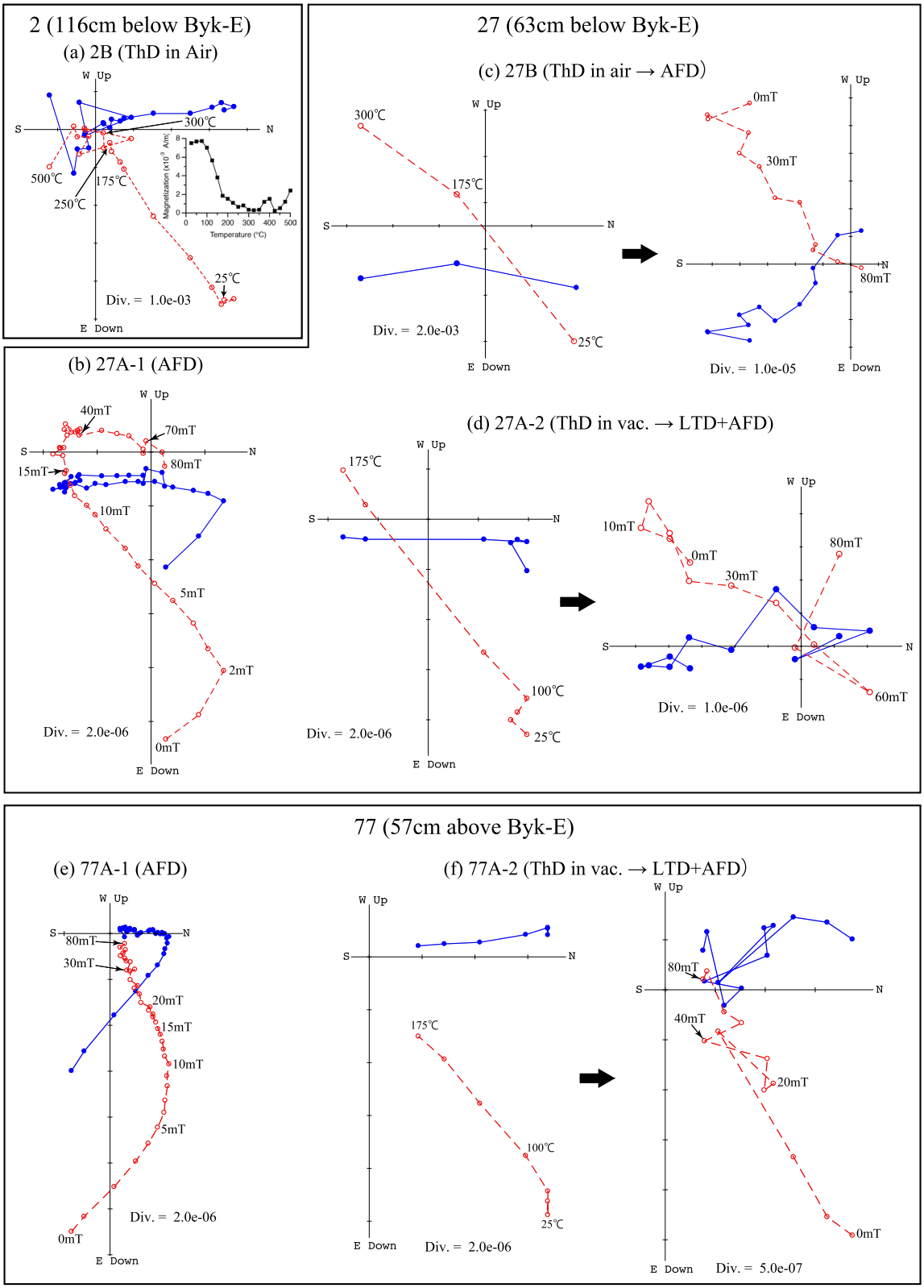

Fig. 3 (See legend on previous page.)

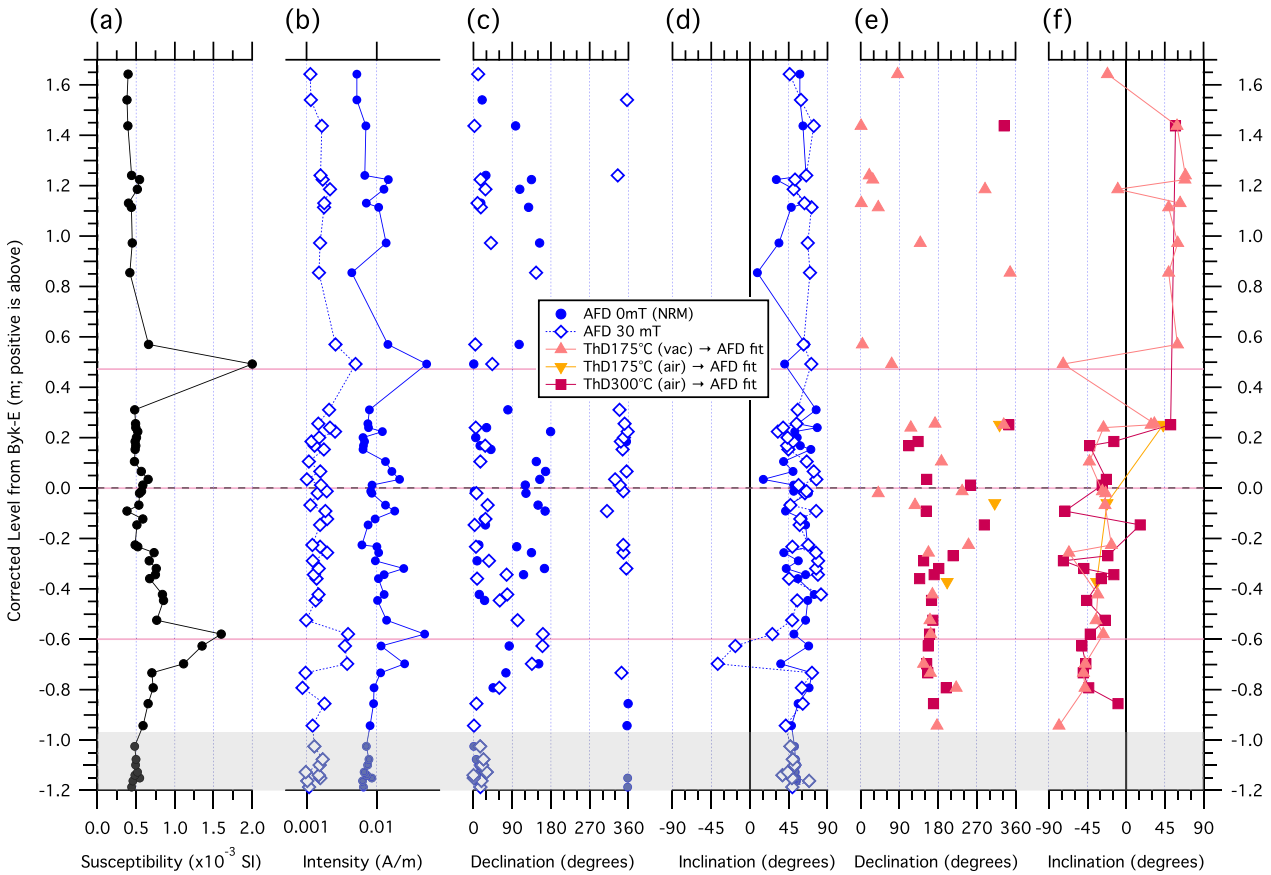

Fig. 4 Paleomagnetic results plotted versus levels above or below the Byk-E tephra layer (corrected for the slope of the outcrop). **a** Volume magnetic susceptibility for average of A and B specimens (see Additional file 6: Table S1a), **b** magnetization intensity, **c** declination, and **d** inclination for A specimens used for PAFD experiments (see Additional file 6: Table S1a). Blue solid circles and blue open diamonds are NRM before demagnetization and after AFD at 30 mT, respectively. **e** Declination, and **f** inclination for samples used for PAFD experiments following thermal demagnetization. Pink triangles are the results of PCA linear fitting on PAFD results following PThD experiments up to 175 °C in vacuum. Orange inverted triangles and red squares are the results of PCA linear fitting on PAFD results following PThD experiments at 175 °C and 300 °C in air, respectively. Three tephra layers identified in this study are shown as horizontal lines. For the results of PCA, only samples yielding MAD less than 15° are shown. Gray shading for levels between −95 cm and −120 cm represents the interval with no reliable magnetization due to unavailability of thermal demagnetization followed by PAFD experiments

minerals due to laboratory heating. Magnetic susceptibility is reduced by further heating to temperatures between 440 and 560 °C. The increase and subsequent decrease of magnetic susceptibility with a peak around 440–480 °C during heating in air might be originated from production of superparamagnetic magnetite by oxidation of sulfide minerals and further oxidation to hematite. Thermal alteration of sediment samples during laboratory heating in air will be discussed in detail in subsection 'laboratory heating experiments' in the "Discussion" section.

Magnetic hysteresis and FORC

The hysteresis parameters of the measured samples are listed in Table 2. Figure 7 shows a Day plot for the ratios of the hysteresis parameters (Day et al. 1977). The values of the measured samples could not be explained by a mixture of SD and MD magnetite (Fig. 7a). On the other hand, these values fall within the region of mixtures between single domain (SD) and superparamagnetic (SP) magnetite with particle sizes between 5 and 10 nm (red curves in Fig. 7b; Dunlop et al. 2002). The measured values also fall within the area of greigite-bearing marine sediments with diagenesis (colored area in Fig. 7b; Roberts et al. 2011). Alternatively, the measured values were compared with those calculated using micromagnetic simulations for greigite (Fig. 7c; Valdez-Grijalva et al. 2020). It is suggested that the measured values are also consistent with those for non-interacting greigite of 80–90 nm grain size.

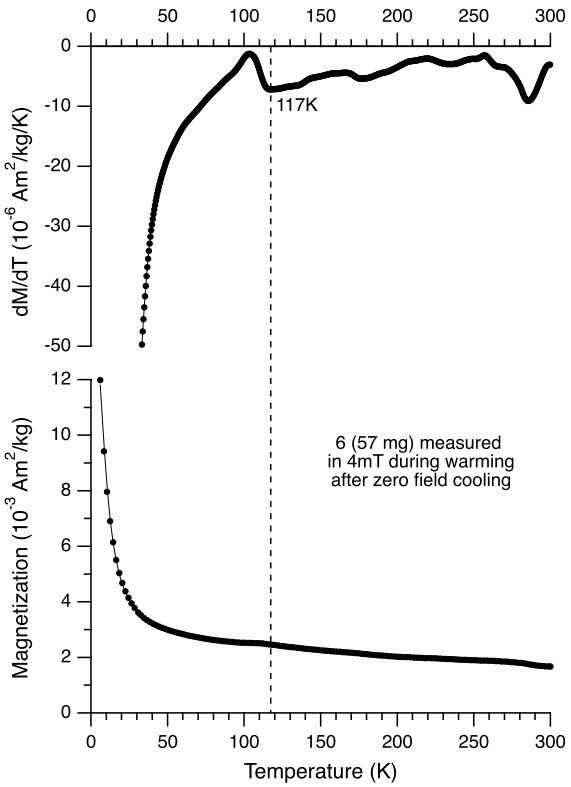

Fig. 5 Low temperature property of sample 6 measured with MPMS. Magnetization (magnetic moment) was monitored during warming in 4 mT field following zero field cooling (bottom). The curve after differentiation (above) clearly shows inflection point at ~ 117 K

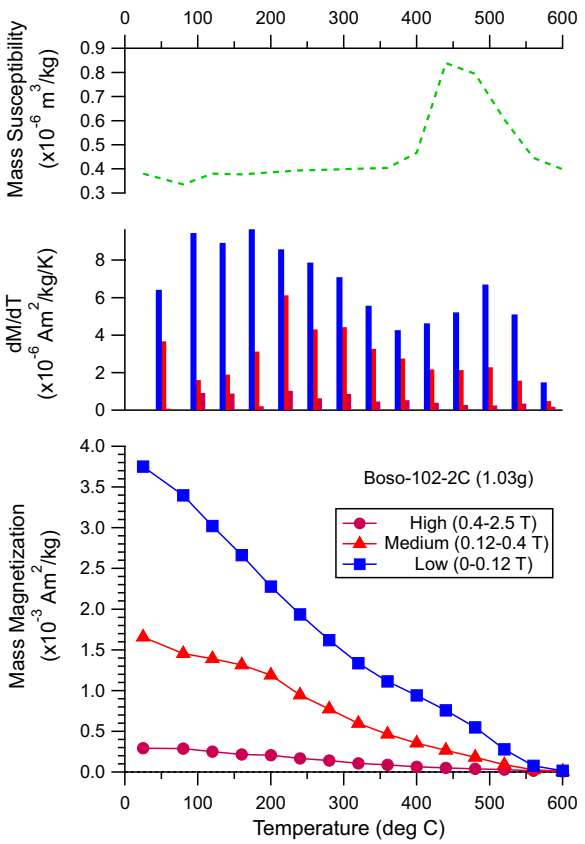

Fig. 6 An example of thermal demagnetization of three-component IRM experiments based on Lowrie (1990). Bottom diagram shows the magnetization for high (red circles; 0.4–2.5 T), medium (pink triangles; 0.12–0.4 T) and low (blue rectangles; 0–0.12 T) coercivity components after each heating step in air. Middle diagram shows the magnetization removed at each heating step for high (red), medium (pink) and low (blue) coercivity components. Top diagram shows the magnetic susceptibility measured after each heating step

The results of the first-order reversal curve (FORC) measurements of the selected samples are shown in Fig. 8. Figure 8e and j shows the results for the samples taken from the sediments containing tephra C (sample 30–4) and A (sample 76–1), respectively. The FORC diagrams are typical of marine sediments with central ridge along horizontal axis and a moderate vertical spread close to vertical axis (e.g., Roberts et al. 2018b). The FORC diagrams suggest that the interactions between the magnetic particles are moderate, but not strong. To determine the magnetic mineral components in the sediments of the outcrop, we conducted FORC PCA (Fig. 9; Harrison et al. 2018). A 94% variance is explained by two principal components, PC1 and PC2 (Fig. 9a). Figure 9b shows a plot of PC2 versus PC1. Based on the plots, the samples can be explained by three end members, EM1, EM2, and EM3. FORC diagrams for EM1, EM2, and EM3 are shown in Fig. 9c, d, and e, respectively. The horizontal profiles for EM1, EM2, and EM3 are also shown in Fig. 9f, g, and h, respectively. EM1 is very close to sample No. 12 (Fig. 8l; 89-2), which has a relatively long central ridge up to ~ 250 mT. The negative region is obvious around $B_c = 0$ and the vertical spread along B_u is small, indicating a lower contribution of multidomain grains. EM2 is very close to sample No. 10 (Fig. 8j; 76-1) corresponding to tephra A, which has a short and subdued central ridge up to ~ 80 mT. The vertical spread along B_u is large, suggesting a higher contribution of multidomain titanomagnetite and/or magnetite. EM3 is close to sample No. 5 (Fig. 8e; 30-4) and No. 6 (Fig. 8f; 39-1), which has a central ridge up to ~ 150 mT. The vertical spread along B_u may indicate a moderate contribution of multidomain titanomagnetite and/or magnetite.

Discussion

Magnetic minerals

Based on electron microscope observations (Fig. 1a, c, d f, and g), we identified titanomagnetite as ferrimagnetic iron oxides in the sediments. Moreover, the observation of the Verwey transition (Fig. 5) confirms

Table 2 Hysteresis parameters (B_{cr}, B_c, M_{rs}, and M_s) of 12 selected samples

No	Sample	Weight (mg)	B_{cr} (mT)	B_c (mT)	M_{rs} (Am^2)	M_s (Am^2)	M_{rs}/M_s	B_{cr}/B_c
1	1-1	24.2	56.9	15.1	1.04E−07	6.66E−07	0.156	3.768
2	7-1	10.0	62.9	18.6	6.12E−08	3.03E−07	0.202	3.383
3	10-4	15.8	57.0	14.3	7.56E−08	4.73E−07	0.160	3.989
4	18-2	23.3	49.6	12.9	1.25E−07	7.80E−07	0.160	3.848
5	30-4	å	38.6	10.8	2.47E−07	1.90E−06	0.130	3.573
6	39-1	13.0	49.8	12.3	5.77E−08	3.67E−07	0.157	4.050
7	53-1	37.9	55.3	14.5	2.04E−07	1.16E−06	0.176	3.810
8	63-2	17.5	53.7	14.6	1.18E−07	7.30E−07	0.162	3.676
9	70-3	9.3	57.0	16.7	4.66E−08	2.34E−07	0.199	3.411
10	76-1	53.8	30.6	6.5	6.16E−07	6.59E−06	0.093	4.712
11	80-1	12.8	67.8	18.5	7.08E−08	3.38E−07	0.209	3.664
12	89-2	30.8	69.2	21.8	1.49E−07	6.38E−07	0.234	3.172

the existence of low-Ti magnetite in the studied sediments. Thermal demagnetization experiments of three-axis IRM (Fig. 6) for low coercivity component are also consistent with this finding, suggesting the presence of a magnetic mineral component with unblocking temperatures of ~ 560 °C. The observation of titanomagnetite grains might be consistent with the fact that the low coercivity component shows a broad decrease around 200–400 °C.

FORC diagrams (Fig. 8) and FORC PCA analysis (Fig. 9) show that there is a central ridge in the typical coercivity range of several tens of mT and 100 mT, suggesting the presence of non-interacting SD magnetite/titanomagnetite as well as MD magnetite/titanomagnetite (EM2; Fig. 9d). In addition, there might be possible minor contribution of SD and MD greigite grains for EM2 and EM3 (see Fig. 2 and discussions in the following paragraph for SD greigite grains). The contribution of non-interacting SD magnetite may possibly originate from detrital grains and/or fossil magnetotactic bacteria. The FORC diagrams for EM2 (Fig. 9d) and EM3 (Fig. 9e) with significant signatures in the region of negative B_u around $B_c = 30$ mT may also suggest that magnetite contributes to the vortex state (pseudo-single domain).

Thermal demagnetization experiments of the three-axis IRM for the medium coercivity component show a significant decrease around 200–300 °C, which is consistent with the observation of greigite in the sediments. FORC PCA analysis (Fig. 9) revealed that EM1 has a relatively long central ridge up to ~ 250 mT, which might be an indication of the presence of greigite as SD particles. Greigite might be present as vortex state particles, which is evidenced by a considerably broadened distribution around $B_c = 30$–120 mT. Although the interpretation of the Day diagram is not straightforward (e.g., Roberts et al. 2018a), the distribution on the diagram is consistent with the area of greigite bearing marine sediments (Fig. 7b).

A striking feature of the thin sections is the strong oxidation observed in the outer part of framboidal pyrite (Fig. 1a, b, c and e). The elemental distribution pattern obtained by EDS suggests that iron remained in the pyrite grains, whereas sulfur in the pyrite grains in the outer part of the framboid was almost completely replaced with oxygen. The replacement of sulfur by oxygen depends on the grain size, the size of the framboid, and the surrounding conditions in the sediment. It has been reported that oxidative weathering of pyrite to an iron (oxyhydr)oxide (either ferrihydrite

(See figure on next page.)

Fig. 7 Day plots of the measured and compiled hysteresis parameters. **a** Day plot (Day et al. 1977) of the measured hysteresis parameters (black circles). Numbers correspond to those in Table 2. Nos 5 and 7 are tephra C and A, respectively. SD, PSD and MD shown in blue are domain states corresponding to magnetite. Blue curves and numbers are two SD-MD mixing curves and mixing ratios (Dunlop et al. 2002). **b** Day plot of the parameters for the measured samples (black circles) together with that for greigite bearing marine sediments around New Zealand (Roberts et al., 2011). Red curves are mixing curves of SD with 5 nm and 10 nm SP particles and with mixing ratios (Dunlop et al. 2002). **c** Day plot for framboidal greigite based on micromagnetic simulations (replotted from Valdez-Grijalva et al. 2020). Open circles are non-interacting grains of different sizes (the left most circles and the right most circles correspond to 30 nm and 100 nm, respectively). An open rectangle is a framboid with 30 nm particles. Upward-pointing and downward-pointing triangles are mixtures of framboids with isolated SD grains and isolated SV (single vortex) grains, respectively. The mixtures contain increasing proportions of SD and SV material from 10 to 100% with grain size contributions of 30–48 nm and 70–80 nm

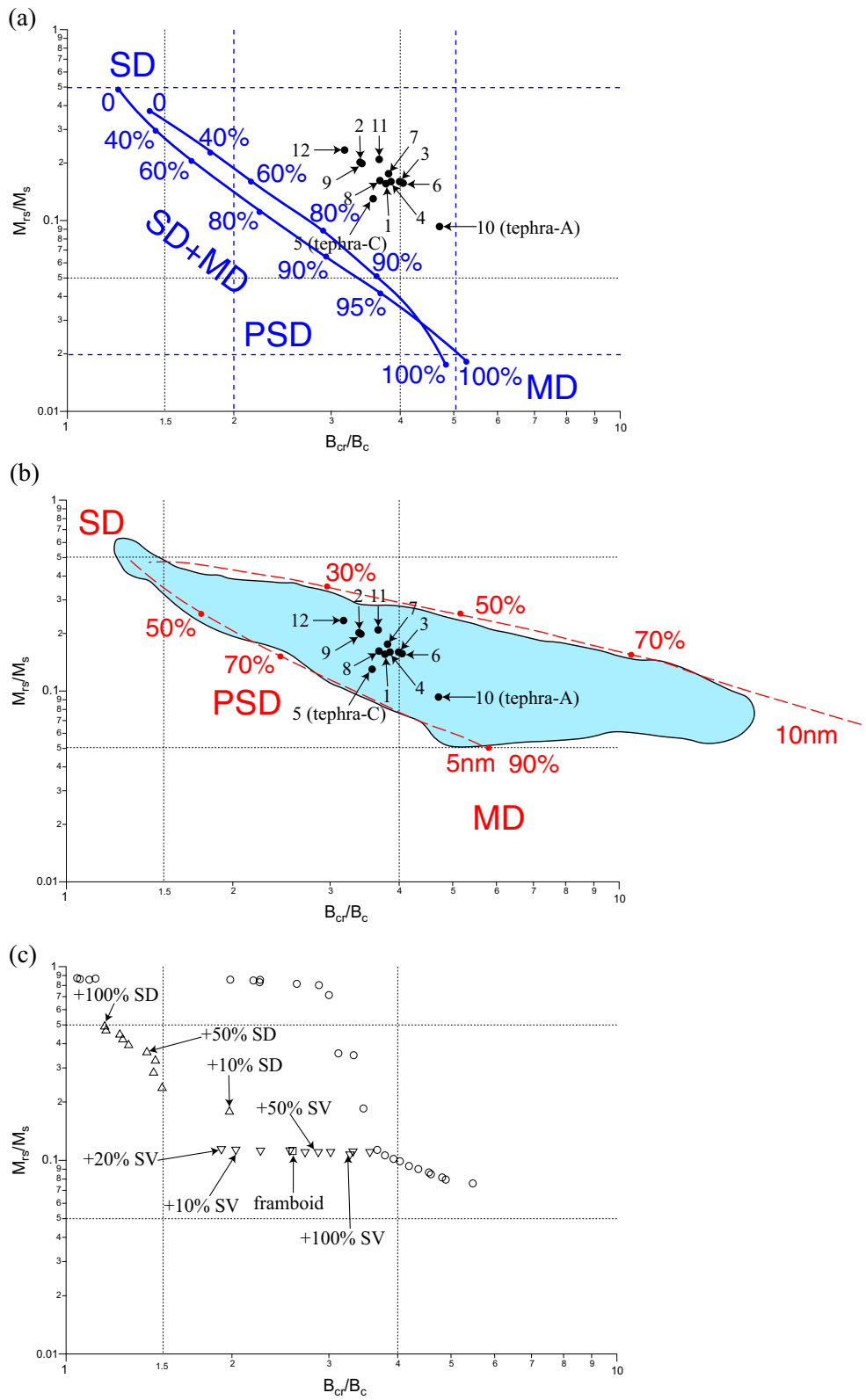

Fig. 7 (See legend on previous page.)

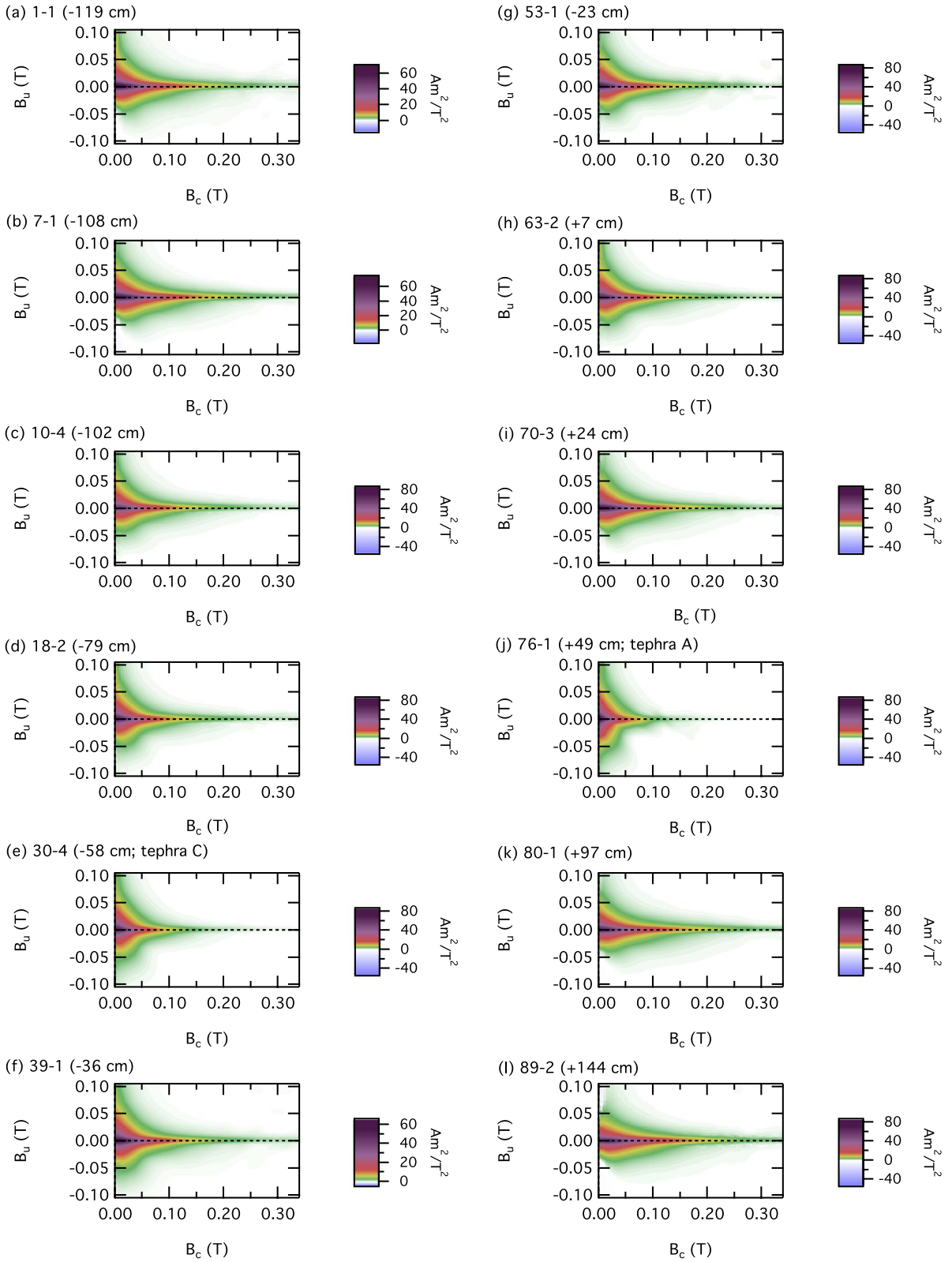

Fig. 8 Results of first order reversal curve (FORC) measurements for 12 selected samples. Specimens 30-4 (**e**) and 76-1 (**j**) are tephra C and tephra A, respectively

$[(Fe^{3+})_2O_3 \bullet 0.5H_2O]$ or feroxyhyte [δ-$Fe^{3+}O(OH)$]) is ubiquitous in sediments buried deep and not exposed to the land surface (Gu et al. 2020).

Feroxyhyte is a planar antiferromagnet with the net sublattice moments aligned parallel or antiparallel to c-axis (Koch et al. 1995). Each particle acquires a net moment due to small number of layers along the c-direction, and the presence of surface steps causing the formation of ferrimagnetic domains with an odd number of layers. The Curie temperature, saturation magnetization, and IRM after saturation for a synthetic feroxyhyte are reported as 182 °C, 14 Am^2/kg, and 6.7 Am^2/kg, respectively (Koch et al. 1995). Considering the observation of pyrite oxidation by electron microscopy and the evidence that there is substantial loss of magnetization by thermal demagnetization at 175 °C (e.g., Fig. 3a), feroxyhyte could be one of the principal magnetic minerals in the studied sediments, which might have acquired secondary magnetization after the sediments changed to the oxidative condition associated with the uplifting of the Boso Peninsula. The absence of a concentric distribution of FORC diagrams representative of interacting SD greigite is considered to result from partial oxidation of the outer shell, which will be explained in the next paragraph. This interpretation is also consistent with the distribution on the Day diagram for a theoretical curve for non-interacting greigite particles (open circles; Fig. 7c).

Although the contribution of the total magnetization is minor, thermal demagnetization experiments of three-axis IRM for high coercivity component (Fig. 6) show a gradual decrease during heating up to 600 °C. This may be attributed to the presence of hematite with distributed unblocking temperatures. There is no evidence of unblocking temperatures indicative of goethite (α-FeOOH) lower than its Curie temperature of ~ 120 °C (e.g., Ozdemir and Dunlop 1996).

Laboratory heating experiments

To understand the coercivity distributions of magnetic minerals contributing to magnetizations in the sediments and laboratory alteration during heating, a series of heating experiments were conducted. The first half of the experiment comprises ARM measurements during sample heating in air according to the protocol that resembles the microcoercivity unblocking temperature diagram proposed by Sato et al. (2019). First, ARM heating experiments were performed on selected samples in air. The ARM is acquired before each heating step, which is AF demagnetized and plotted in Fig. 10a. The coercivity spectrum of magnetization remaining after each heating step was calculated by taking the derivative of Fig. 10a in terms of coercivity (Fig. 10b). The coercivity spectrum indicates that the peak coercivity is centered around 25 mT, which was reduced to < 80% by heating up to ~ 200 °C. This is consistent with the reduction in the magnetization intensity observed during PThD experiments (Fig. 3a). The magnetization centered at approximately 25 mT was further reduced to < 70% by heating up to ~ 300 °C, which is also consistent with the PThD experiments. Coercivity after heating above 300 °C shows a considerably broad spectrum extending from 5 to 75 mT, which was gradually reduced to zero above ~ 550 °C.

After AFD following each heating step, ARM is acquired, followed by AFD to identify the thermal alteration during heating (Fig. 10c), and the corresponding coercivity spectrum was calculated (Fig. 10d). The diagram shows that the coercivity of heating products (distribution in Fig. 10b should be subtracted from that in Fig. 10d to observe the actual thermal alteration effect on magnetization) is prominent in the range of 5 mT and 35 mT. The heating product steadily increased with increasing temperature up to ~ 400 °C. Heating above ~ 400 °C to ~ 500 °C produced a significant amount of heating induced magnetic materials, which was slightly reduced by heating above ~ 500 °C up to ~ 550 °C. It should be noted that the spectrum in Fig. 10b is not purely representative of the coercivity distributions of the natural state before heating because ARM was acquired repeatedly after each heating step, introducing a minor amount of magnetization of the heating products. However, this effect could be ignored assuming that the magnetization of the heating product was not significant relative to the total magnetization and that the unblocking temperatures of the heating products were mostly lower than the corresponding temperature during the experiments.

The second experiment was composed of a set of measurements using VSM during the stepwise heating of a sediment sample in air. After each heating step, the hysteresis parameters were measured, followed by FORC measurements. Figure 11a shows plots of hysteresis measurements versus temperature. B_{cr} gradually decreases from ~ 200 °C to ~ 400 °C, and then decreases significantly at 450–500 °C followed by a linear increase at 600 °C. B_c shows a gradual decrease from ~ 25 °C to 400 °C and a sudden increase at 450 °C, followed by a slight decrease from 500 °C to 600 °C. M_{rs} decreases slightly from 200 °C to 400 °C, increases suddenly at 450 °C, and then decreases from 500 °C to

(See figure on next page.)

Fig. 9 Results of FORC PCA (Harrison et al. 2018) on 12 samples. **a** Variance explained by principal components (solid circles) is shown together with cumulative variance (blue columns). 94% of variance is explained with PC1 and PC2. **b** FORC for each sample is plotted on PC2 versus PC1 diagram together with end members EM1, EM2 and EM3. FORC diagrams are shown for **c** EM1, **d** EM2 and **e** EM3. Color scales for **d** and **e** are the same as **c**. Horizontal profiles on FORC diagrams along $B_u = 0$ are shown for **f** EM1, **g** EM2 and **h** EM3

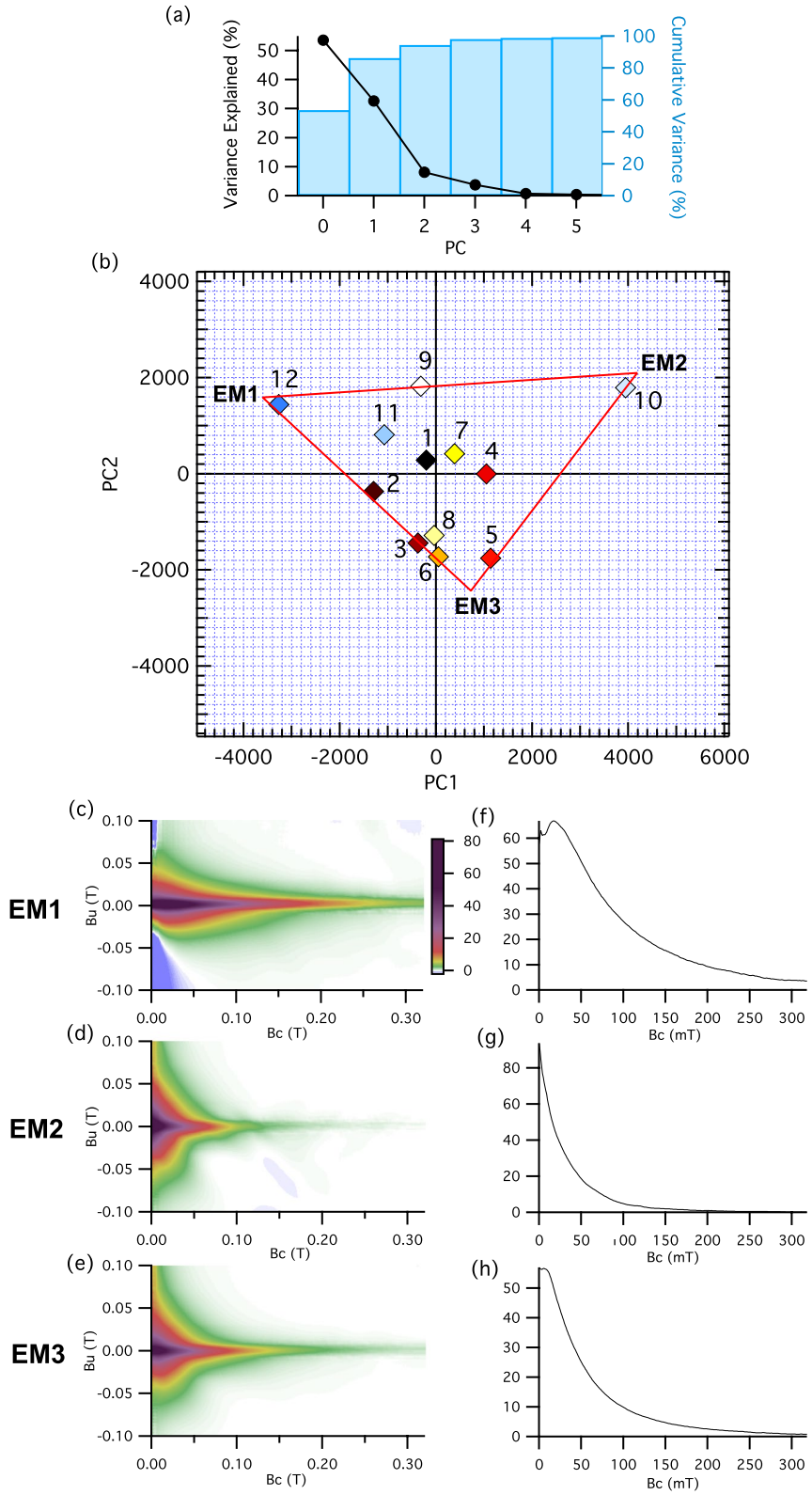

Fig. 9 (See legend on previous page.)

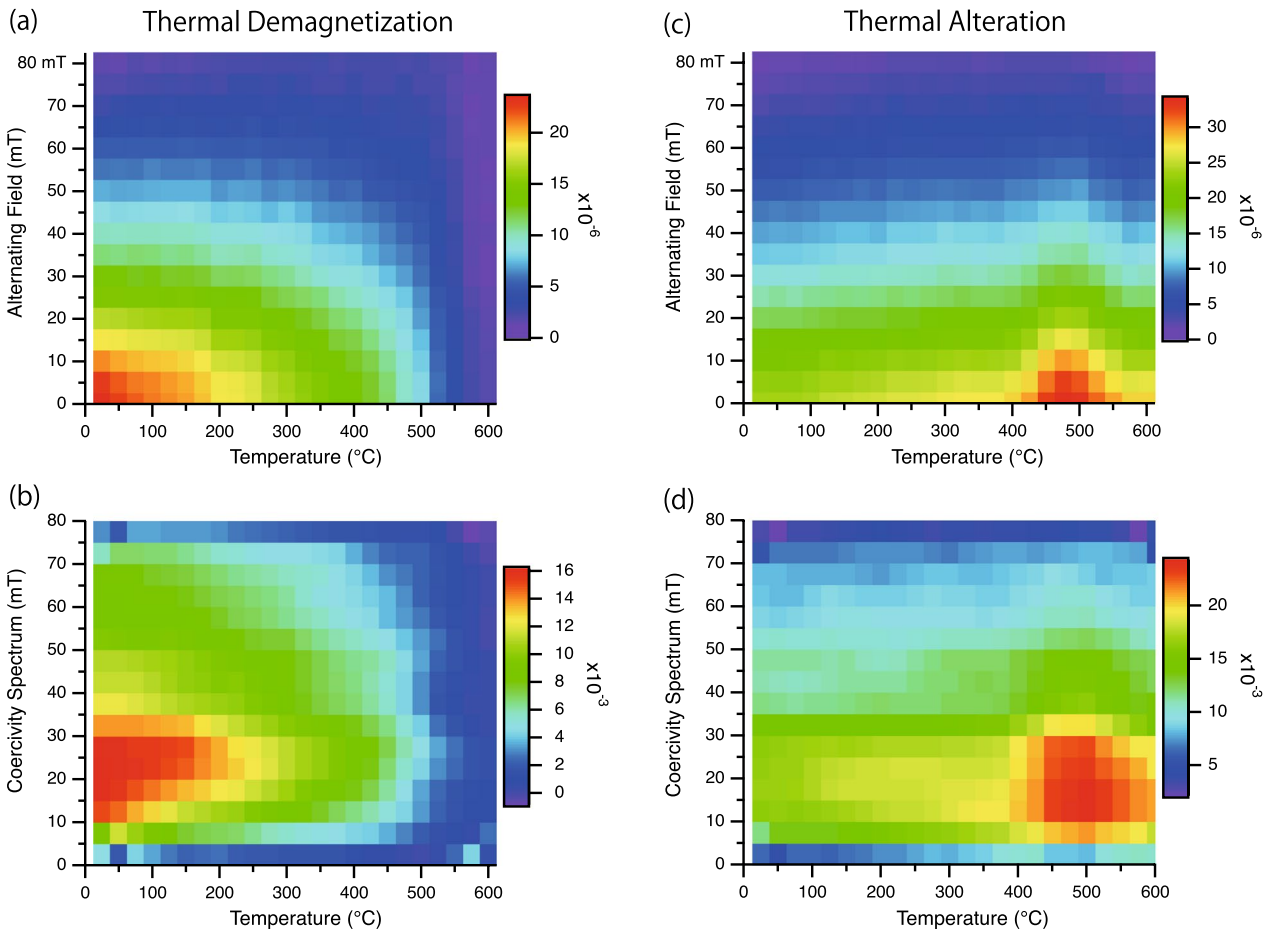

Fig. 10 Coercivity spectrums of ARM monitored during heating of sample 102-1Z-1-B. **a** The first ARM is acquired before each heating step, which is AF demagnetized and the magnetization is plotted with color for the corresponding temperature and field steps. **b** Coercivity spectrum of magnetization after each heating step is obtained by dividing the magnetization difference of successive AFD steps by the AFD step difference in **a**. **c** The second ARM is acquired and PAFD demagnetized up to 80 mT after removal of the first ARM by AFD up to 80 mT following each heating step, which is useful in identifying thermal alteration. **d** Coercivity spectrum of magnetization in **c**. ARM acquisition was conducted with DC field of 50 μT and AC field of 80 mT

600 °C. M_s decreases slightly from 200 °C to 400 °C and then increases suddenly at 450 °C, followed by a decrease to 550 °C. Figure 11b shows a Day plot of the hysteresis parameters. Before heating (25 °C), the data on the plot are in the region of MD grains ($B_{cr}/B_c \sim 6$, $M_{rs}/M_s \sim 0.3$). The data points move slightly toward the right where B_{cr}/B_c is ~7 at 300 °C and then back to the left where B_{cr}/B_c is ~6.5 at 400 °C. Then, the data points move significantly to the upper left ($B_{cr}/B_c = \sim 3.5$, $M_{rs}/M_s = \sim 0.5$) at 450 °C and move slightly in the same direction ($B_{cr}/B_c = \sim 3$) at 500 °C. The data point at 550 °C moves to the right ($B_{cr}/B_c = \sim 4.5$) along the same trend as that between 400 °C and 450 °C, then further moves to the right ($B_{cr}/B_c = \sim 5.3$) at 600 °C.

Figure 12 shows a series of FORC diagrams during stepwise heating in air. The diagrams show a gradual shrinkage of the central ridge from 25 °C to 400 °C, followed by a clear stepwise change between 400 °C and 450 °C. The diagram further changed from 450 to 600 °C. The serial change of the FORC diagram during heating was better captured by FORC-PCA analysis (Fig. 13). Up to 97% of the total variance of FORCs could be explained by two principal components, PC1 and PC2 (Fig. 13a). The FORC diagrams are explained by three end members, EM1, EM2, and EM3 (Fig. 13b). The FORC starts from around EM1 (25 °C in Fig. 13b), then moves gradually to around EM2 with increasing temperatures up to 400 °C. By heating to 450 °C, the FORC suddenly moved to EM3, which was also recognized by direct observation of the two FORC diagrams. The FORC stays around EM3 for a temperature of 500 °C, and then moves stepwise back to EM2 up to a temperature of 600 °C.

FORC diagrams corresponding to EM1, EM2, and EM3 are shown in Fig. 13c–e, respectively. The horizontal profiles of the FORC diagrams along $B_u = 0$ for EM1, EM2,

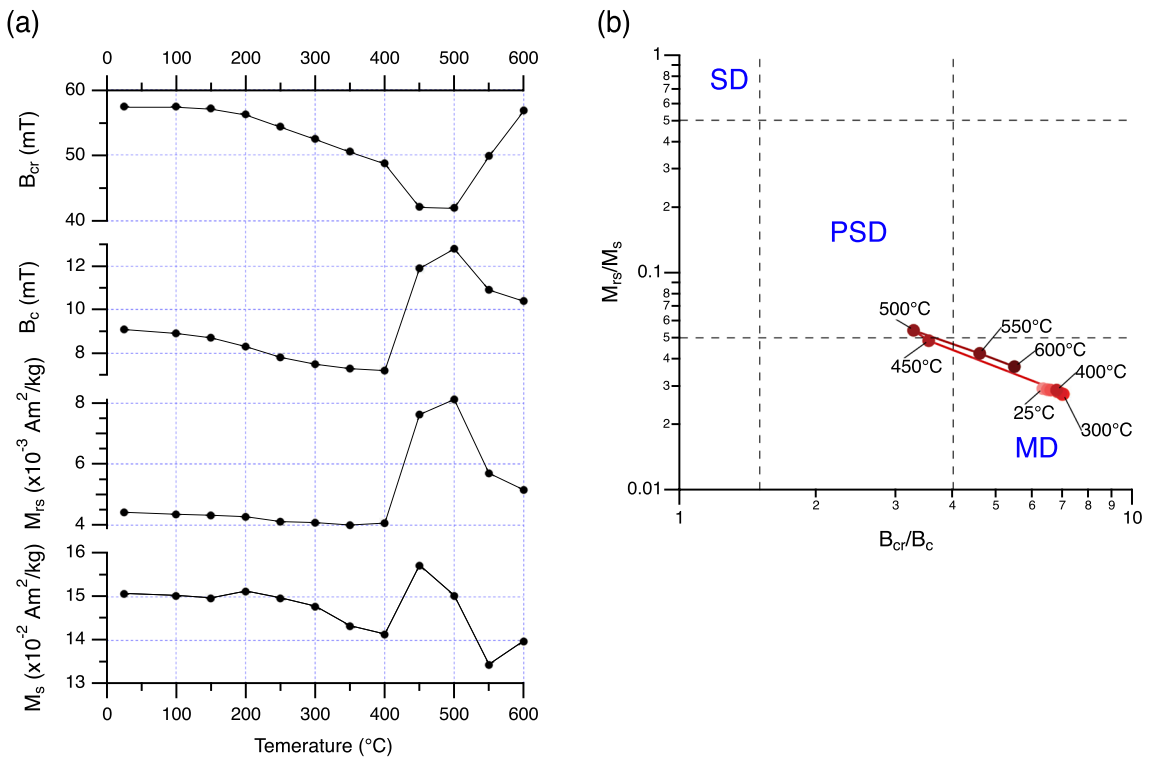

Fig. 11 Change of hysteresis parameters during heating. **a** Hysteresis parameters during heating in air of sample 102-1Z-3. **b** Day plot for the hysteresis parameters during heating

and EM3 are also shown in Fig. 13f–h, respectively. EM1, which corresponds to the FORC diagram before heating, is characterized by an extended central ridge up to $B_c \sim 300$ mT (Fig. 13c and f). The higher coercivity of the central ridge could be attributed to the presence of SD greigite. EM2 (representative of FORC after heating to 400 °C) is characterized by a subdued central ridge extending to $B_c \sim 200$ mT (Fig. 13d and g), which may suggest the decomposition of greigite by heating. The negative region for $B_c \sim 0$ mT and $B_u < \sim -5$mT typical for the FORCs of EM2 and EM3 (Fig. 13d and e), which is clearly recognized for FORCs at temperatures above 350 °C (Fig. 12), might be associated with SD magnetite and greigite (Roberts et al. 2014). A slight increase in the central ridge of EM2 around 400 °C, just close to the origin ($B_c \sim 0$ mT; Fig. 13g) may suggest the production of superparamagnetic particles by heating, possibly due to the decomposition of feroxyhyte and/or greigite. Removal of SD greigite and/or production of SP particles is also consistent with a slight shift from 25 °C to 400 °C on the Day diagram to the lower right (Fig. 11b).

EM3 corresponding to temperature of 450–500 °C is characterized by subdued central ridge extending to $B_c \sim 150$ mT (Fig. 13e and h). Another feature is a bump appearing on the central ridge at approximately 30 mT suggesting the production of magnetic particles (Fig. 13h). In addition, a characteristic positive region on the FORC diagram around $B_c \sim 40$ mT and $B_u \sim -50$ mT appeared, which was not obvious for EM1 and EM2. This might be due to the production of magnetic particles by heating, some of which could interact with each other. The production of magnetic particles could be best visualized by the previous ARM diagram for 400–550 °C and ~ 10–30 mT (Fig. 10d). The shift to the PSD region in the Day diagram at 450–500 °C is also consistent with the interpretation that (possibly interacting) SD particles are produced by heating. Finally, the FORC moves from EM3 back to EM2 (Fig. 13b), which may suggest that the particles produced by heating to 450–500 °C were decomposed by heating to 600 °C. The removal of magnetic particles produced by heating at 450–500 °C could also be observed on the ARM coercivity diagram (Fig. 10d) and the Day diagram (Fig. 11b). The magnetic particles produced by heating at 450–500 °C could be interpreted as magnetite and the removal of the signal by heating further to 600 °C could be considered to be due to the oxidation of magnetite to hematite, which has much less magnetization than magnetite.

Microcoercivity unblocking temperature diagram experiments using AF demagnetization of ARM acquired

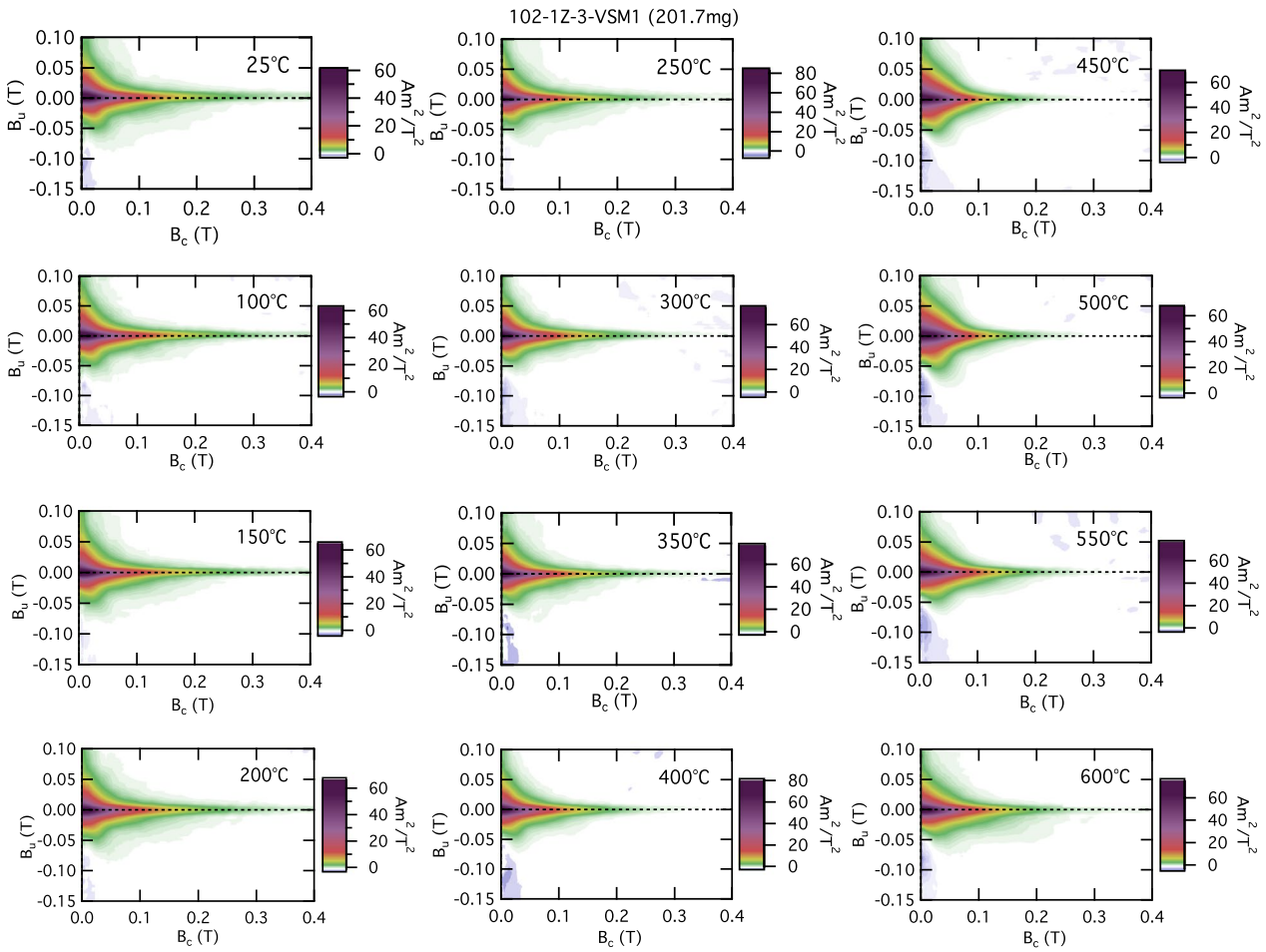

Fig. 12 Results of first-order reversal curve (FORC) measurements for sample 102-1Z-3 during stepwise heating in air

before each temperature step (Sato et al. 2019) combined with thermal alteration monitoring using ARM acquired after each temperature step is a powerful tool for understanding the coercivity spectrum at each unblocking temperature due to newly produced magnetic minerals by heating. It should be noted that this method is valid, assuming that the unblocking temperature of newly produced magnetic minerals is usually less than the heating temperature that produces the secondary magnetic minerals. On the other hand, FORC and FORC PCA of stepwise heating of sediment samples provide detailed information on the changes in the magnetic mineral and domain state during heating in the laboratory. Van Velzen and Zijderveld (1992) proposed monitoring the coercivity spectrum of the IRM during stepwise thermal demagnetization. Alternatively, Torii et al. (1996) proposed a method to apply SIRM before and after each laboratory heating step to monitor unblocking and alteration temperatures, which is similar to the concept of our study of monitoring ARM acquired before and after each heating step. Overall, the combination of two types of laboratory heating experiments using ARM and FORC

(See figure on next page.)

Fig. 13 Results of FORC PCA on a set of FORC diagrams during heating in air for sample 102-1Z-3 shown in Fig. 12. **a** Variance explained by principal components (solid circles) shown together with cumulative variance (blue columns). 97% of variance is explained with PC1 and PC2 and three end members are recognized. **b** FORC for each heating step is plotted on PC2 versus PC1 diagram together with end members EM1, EM2 and EM3. FORC diagrams are shown for **c** EM1, **d** EM2 and **e** EM3. Color scales for **d** and **e** are the same as **c**. Horizontal profiles on FORC diagrams along $B_u = 0$ are shown for **f** EM1, **g** EM2 and **h** EM3. EM1 represents the component before heating. During heating, it gradually moves to EM2 at 400 °C. After 400 °C it moves to EM3 around 450–500 °C then back to EM2 at 600 °C

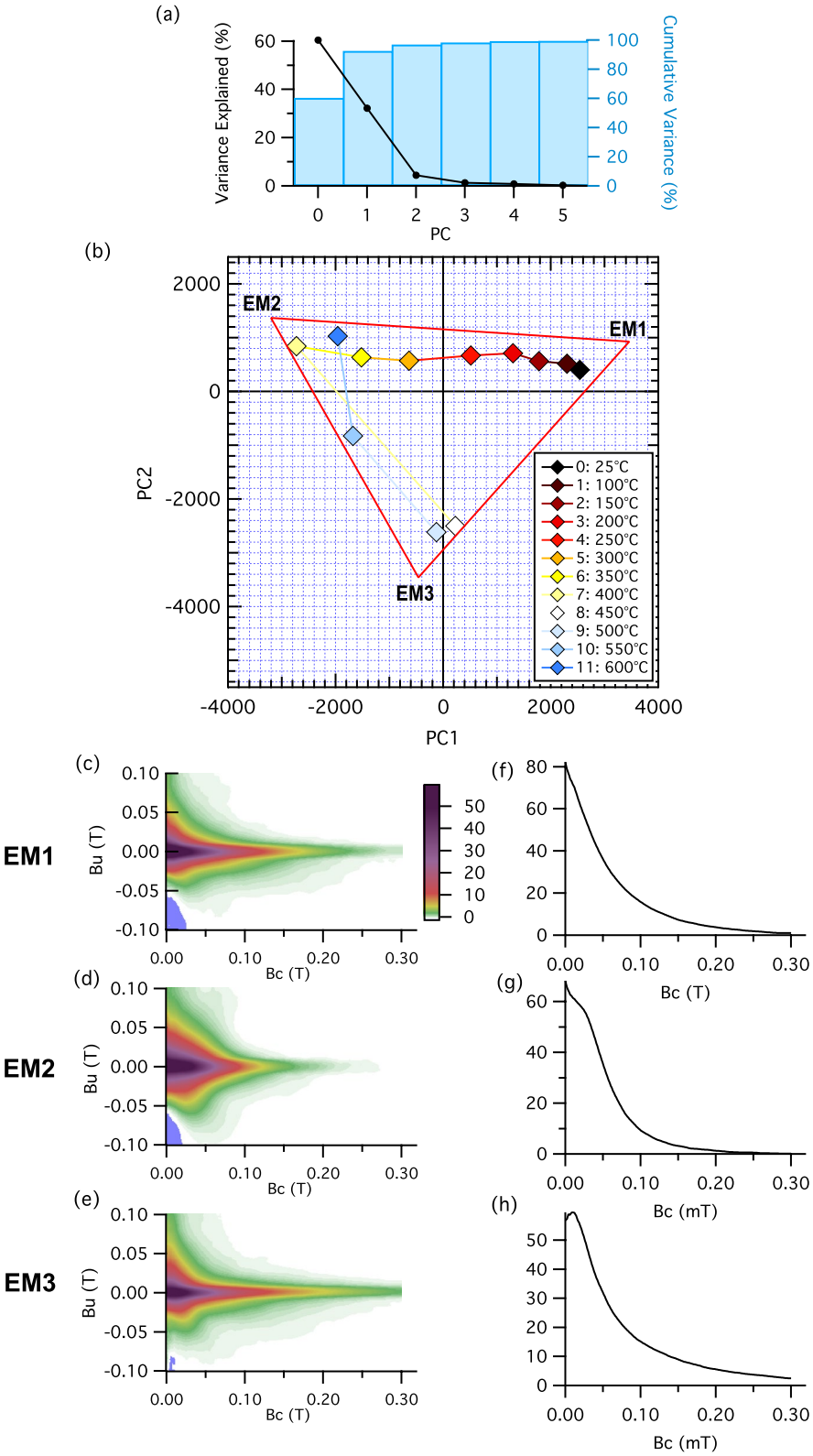

Fig. 13 (See legend on previous page.)

is quite effective in diagnosing unblocking temperatures and thermal alteration critical temperatures for sediments as a complex mixture of magnetic minerals of various origins.

Combined analyses of remagnetization circles

Paleomagnetic directions based on linear regression of the PAFD experiments after heating up to 175 °C and 300 °C are shown in Fig. 4e and f (Additional file 7: Table S2). To maximize the success rate and reliability of paleomagnetic directions, combined analyses of remagnetization circles (McFadden and McElhinny, 1988) were performed on the paleomagnetic results of multiple specimens of each sample drill core (examples are shown in Additional file 5: Figure S5). If there are two components of magnetization with coercivity distributions that do not overlap with each other, we could successfully separate the components by PAFD and linear regression fitting on the corresponding component. On the other hand, if the coercivity spectra of the two components overlap with each other, the demagnetization vector on an equal area projection should fall in a great circle (e.g., Kirschvink 1980). If secondary magnetizations recorded by two specimens have slightly different directions and overlap with the primary magnetization, then the great circles for the directions during progressive demagnetization intersect in the primary direction. Assuming experimental errors or components other than the two components, the great circles may intersect at multiple points. McFadden and McElhinny (1988) formulated to calculate the maximum likelihood estimate of the primary magnetization direction utilizing remagnetization circles.

Figure 14b through d shows the paleomagnetic results based on combined analyses of remagnetization circles by McFadden and McElhinny (1988) using Paleomagnetism.org 2.0 (Koymans et al. 2020). Additional file 7: Table S2 shows the details of lines or great circles of individual specimens fitted with linear regression and the combined analyses of remagnetization circles for each sample. The number of specimens used for the combined analyses of each sample was between two and four. For 22 samples, no reliable line could be obtained by fitting to the directional data of progressive demagnetization (reliability category is '1'). If α_{95} of the mean direction is less than 15° and *t95* is less than 50°, reliability category is '3'. The reliability category of other samples is '2'. VGP latitudes suggest that the directional midpoint of the M–B boundary could be placed at the stratigraphic level between 25 and 55 cm, approximately centered at 40 cm (Fig. 14d). Although samples 91 (195.5 cm) and 93 (208.5 cm) in Fig. 14c show negative inclinations, the comparison of the VGP latitudes with those for Haneda et al. (2020) shows that they are consistent with each other (see Fig. 15e and discussion in the following section).

Correlation with the Chiba section and age model

The paleomagnetic results of the combined analysis of this study were compared with those of the Chiba section (Haneda et al. 2020). In order to facilitate the correlation on various aspects, the relative paleointensity and rock magnetic parameters, including NRM_{30-50}/ARM_{30-50}, k_{LF}, k_{ARM}, $S_{-0.1T}$, $S_{-0.3T}$, used by Haneda et al. (2020) were also measured in this study (Fig. 14e–h; Tables S3 and S4). Haneda et al. (2020) estimated relative paleointensity using NRM and ARM after thermal demagnetization at 300 °C in air. They used a DC field of 0.3 Gauss and an AC field of 80 mT to impart ARM; therefore, we used the same protocol for direct comparison. Then, relative paleointensity was estimated using $NRM_{30-50}/ARM_{30-50} = (NRM_{30}-NRM_{50})/(ARM_{30}-ARM_{50})$ (Fig. 14e; Additional File 8: Table S3), where ARM_x is ARM after AFD at X mT and NRM_x is NRM after AFD at X mT, respectively. They also used k_{LF} and k_{ARM} to calculate k_{ARM}/k_{LF} as a proxy of magnetic grain size (Fig. 14f, g; Additional File 9: Table S4), where k_{LF} is the volume magnetic susceptibility and k_{ARM} is the ARM susceptibility. For the calculation of k_{ARM}, ARM was imparted at DC field of 0.5 Gauss and AC field of 80 mT. S_{ratio} (Fig. 14h; Additional File 9: Table S4) was measured for two field values of −0.1 T and −0.3 T. First, SIRM was acquired with a pulse magnetizer (2G Enterprises Model 660 at GSJ-Lab) and IRMs at 0.1 T and 0.3 T fields were acquired in the opposite direction of the SIRM. The S-ratio for −0.1 T ($S_{-0.1\,T}$) and −0.3 T ($S_{-0.3\,T}$) were calculated as.

$$S_{-0.3T(-0.1T)} = \left(\left(-\,\mathrm{IRM}_{-0.3T(-0.1T)}/\mathrm{SIRM}\right) + 1\right)/2.$$

according to Bloemendal et al. (1992).

In Fig. 15, paleomagnetic and rock magnetic parameters are plotted versus age (black and blue solid circles) in comparison with Haneda et al. (2020) (purple open circles). Age of Byk-E is fixed at 774.1 ka based on Suganuma et al. (2018). The age model according to Haneda et al. (2020) was estimated based on the correlation between oxygen isotope stratigraphy and a sea-level proxy curve obtained from ODP Site 1123, excluding sand layers. The sedimentation rate of the Chiba section excluding sand layers for the interval spanning M–B polarity boundary is 89 cm/kyr (Suganuma et al. 2018), which is applicable for ages younger than 776 ka (1.65 m below Byk-E). On the other hand, the sedimentation rate before 776 ka is 44 cm/kyr (Suganuma et al. 2018). The relative paleointensity variations (Fig. 15d) were used primarily for the correlation with those for Haneda et al. (2020), which is partly assisted by rock magnetic parameters. The best correlation was obtained by assuming

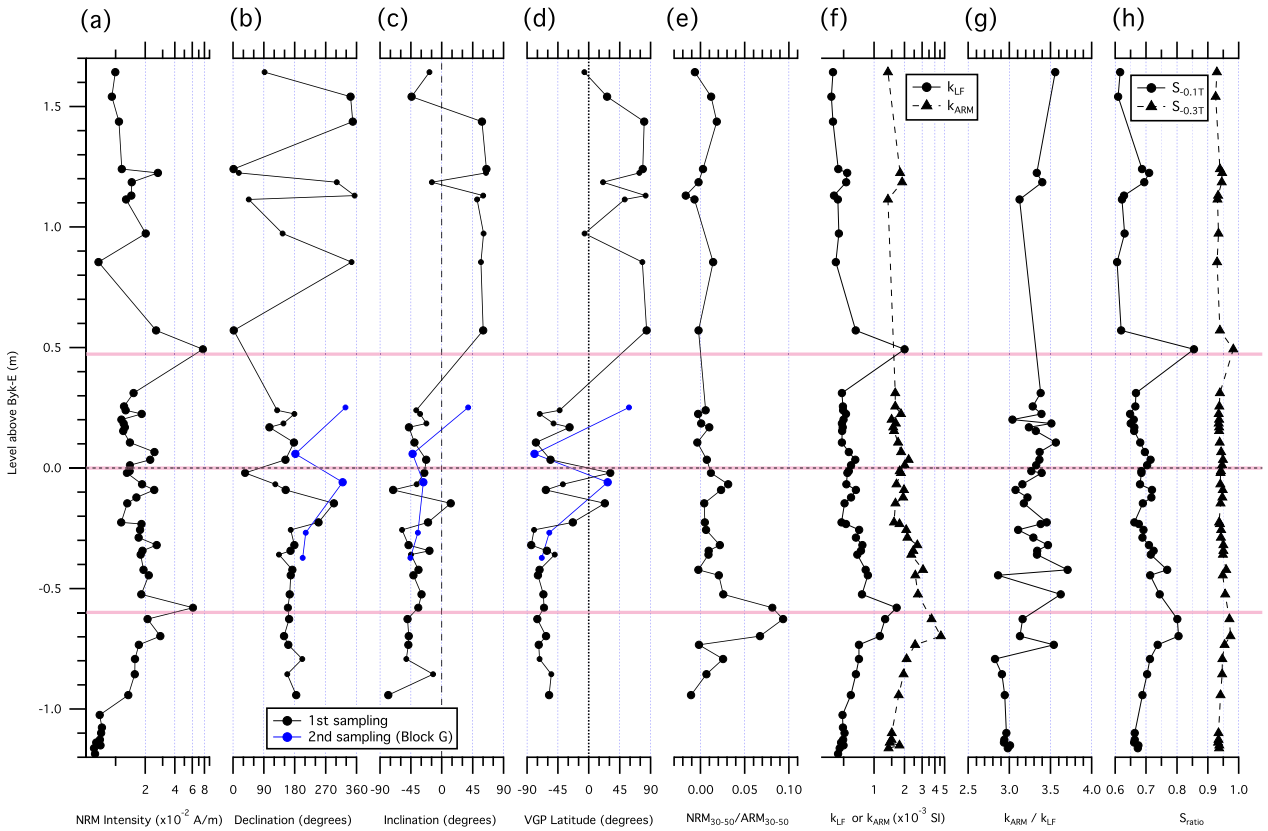

Fig. 14 Paleomagnetic results of combined analyses (Additional file 7: Table S2) plotted versus level above or below the Byk-E key tephra layer (corrected for the slope of the outcrop) together with various rock magnetic parameters. From left to right, **a** NRM intensity, **b** declination, **c** inclination, **d** VGP latitude, **e** relative paleointensity, **f** k_{LF} (solid circles) and k_{ARM} (solid triangles) **g** k_{ARM} / k_{LF}, **h** S_{ratio} ($S_{-0.1\,T}$ and $S_{-0.3\,T}$ shown by solid circles and solid triangles, respectively). Black symbols are the results for the 1st sampling and the blue ones are those for the 2nd sampling (Block G in Additional file 3: Figures S3(c) and S4(e)). In **b**–**d**, reliability categories are expressed by the size of the symbol (the largest is the most reliable category '3'). Horizontal pink lines are tephra layers, which correspond to tephra A, Byk-E tephra, and tephra C from top to bottom, respectively

constant sedimentation rates of 30 cm/kyr and 18 cm/kyr for the intervals above and below the Byk-E tephra layer, respectively. Based on this age model, the ages of tephra A and tephra C are 772.6 ka and 777.5 ka, respectively.

The similarity of VGP latitude variations between this study and that of Haneda et al. (2020) is striking. This could be a confirmation of the reliability of the paleomagnetic directions recorded in the sediments of the studied area and the Chiba section, and hence justifies the applicability of combined analyses of remagnetization circles. k_{LF} and k_{ARM} are considerably different, whereas k_{ARM} /k_{LF} is comparable. S_{ratio} ($S_{-0.1\,T}$ and $S_{-0.3\,T}$) are quite similar to each other for the interval centered around Byk-E. The discrepancy in the concentration

(See figure on next page.)

Fig. 15 Summary of paleomagnetic results and rock magnetic results plotted versus age compared with those by Haneda et al. (2020). From top to bottom, **a** S_{ratio} ($S_{-0.1\,T}$ and $S_{-0.3\,T}$ shown by solid circles and solid triangles, respectively), **b** k_{ARM}/k_{LF}, **c** k_{LF} (solid circles) and k_{ARM} (solid triangles), **d** relative paleointensity (NRM_{30-50}/ARM_{30-50}), and **e** VGP latitude. Details on measurements and calculations of relative paleointensity is explained in the text. Black symbols indicate the results for the 1st sampling and the blue ones those for the 2nd sampling (Block G in Additional file 3: Figure S3(c) and Additional file 4: Figure S4(e)). Large and small symbols (black and blue circles) correspond to the highest (3) and second highest (2) reliabilities (Additional file 7: Table S2), respectively. Purple open circles are paleomagnetic results from Haneda et al. (2020) and small symbols are paleomagnetic data with MAD > 15°. Vertical dashed line is the M–B boundary. Vertical pink lines are tephra layers, which correspond to tephra A, Byk-E tephra, and tephra C from younger to older ages, respectively. Age model for this study is primarily based on the age of Byk-E tephra (774.1 ka; Suganuma et al. 2018) as a fixed point and correlation of relative paleointensity variations with those from Haneda et al. (2020). The best correlation is obtained by assuming sedimentation rates of 30 cm/kyr and 18 cm/kyr for the intervals above and below Byk-E tephra layer, respectively

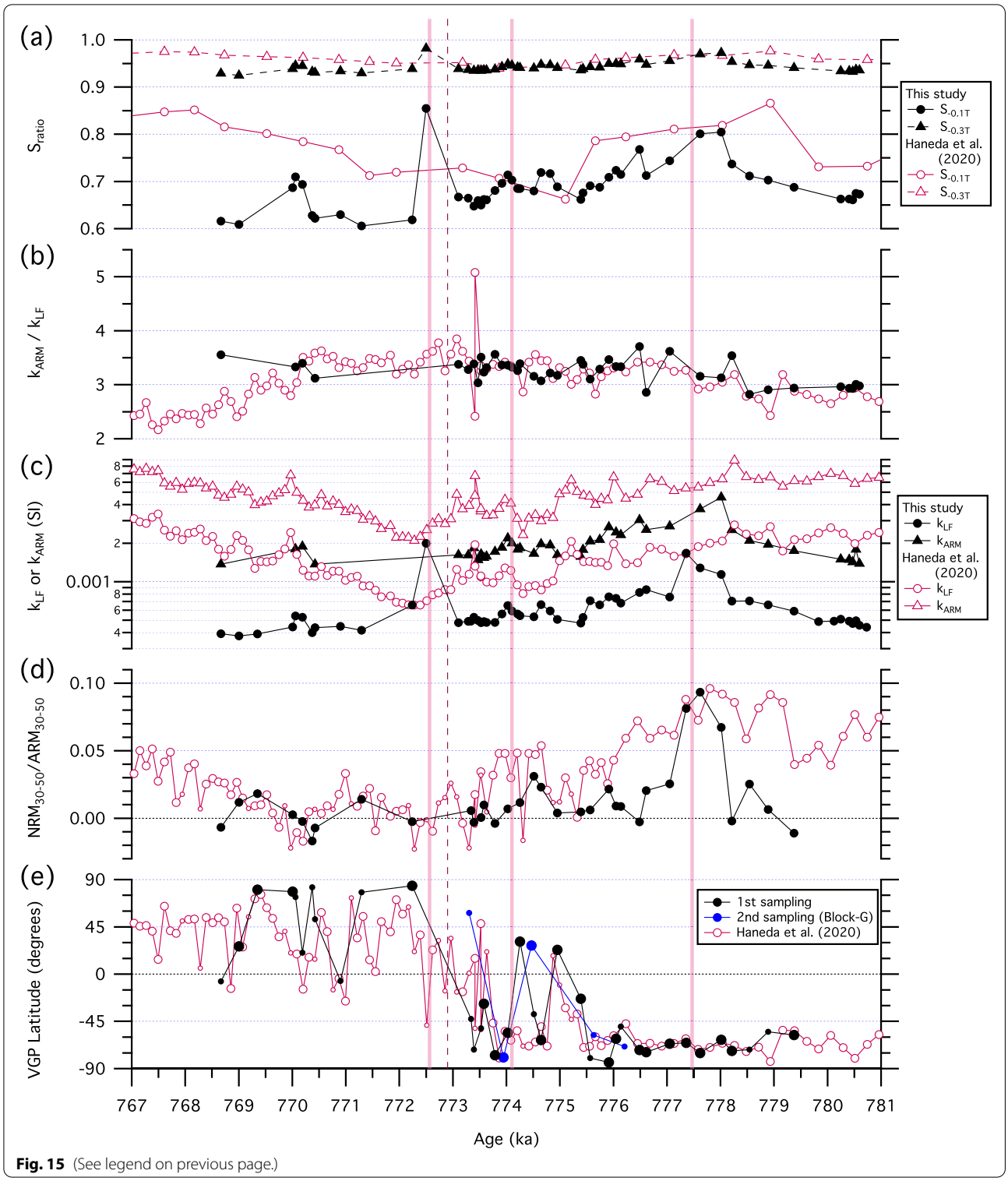

Fig. 15 (See legend on previous page.)

parameters (k_{LF} and k_{ARM}) in spite of the similar values of grain size parameter (k_{ARM} /k_{LF}) may suggest that the studied area had received input of magnetic minerals with similar grain sizes but in smaller amounts. The age for the directional swing from reversed to normal polarities (stratigraphic level of 40 ± 15 cm above the Byk-E tephra) could be estimated as 772.8 ± 0.5 ka using the estimated sedimentation rate of 30 cm/kyr for the

interval above the Byk-E tephra, which is consistent with the age 772.9 ka reported for the Chiba section (Suganuma et al. 2018). The paleomagnetic results obtained in this study show remarkable similarity with those reported by Haneda et al. (2020), which provide an opportunity for one-to-one correlation with a simple model of constant sedimentation rates (Additional file 10).

Conclusions

A high-resolution paleomagnetic record spanning the Matsuyama–Brunhes polarity reversal boundary was obtained from silty clay sediments from an outcrop at Terasaki in the Boso Peninsula, Japan. The following are concluding remarks on identified tephra layers, rock magnetic signatures, and paleomagnetic results:

(1) A tephra layer was identified in the middle of the studied outcrop, which was assigned as the Byk-E tephra (774.1 ka) based on chemical analysis. In addition, two pumiceous tephra layers were recognized 47 cm above and 60 cm below the Byk-E tephra.
(2) Rock magnetic and SEM–EDS analyses revealed that the primary carriers of remanent magnetization were magnetite and titanomagnetite. In addition, greigite was recognized as a diagenetic product in the studied sediment. Furthermore, feroxyhytes may exist as weathering products of pyrite.
(3) Paleomagnetic analyses of the PAFD experiments were not successful in identifying the primary remanent magnetization. PThD experiments suffer from alterations by heating in the laboratory above 175 °C. PAFD experiments following PThD up to 175 °C increased the success rate of extraction of primary magnetizations. To maximize the success rate and reliability of weak magnetization during the polarity transition, combined analyses of remagnetization circles were performed on multiple specimens from each drill core sample. The main directional swing from reversed to normal polarities was recognized at 40 ± 15 cm above the Byk-E tephra.
(4) During stepwise heating in the laboratory, the ARM spectra acquired before and after heating were monitored. A significant reduction in magnetization occurs by heating to 200 °C with a peak coercivity of ~ 25 mT for ARM acquired before heating. Heating to 400 °C resulted in further reduction of magnetization. ARM acquired after heating to 400–500 °C showed a significant increase in the coercivity range of 535 mT, suggesting the production of magnetic minerals by laboratory heating. Furthermore, monitoring of FORC diagrams and FORC PCA analyses revealed a gradual shrinkage of the central ridge extending to $B_c \sim 300$ mT by heating from 25 °C to 400 °C, suggesting the decomposition of SD greigite. Heating to 450 °C introduces a bump centered around 30 mT, which may suggest the formation of aggregates of SD magnetic minerals with interactions.
(5) The paleomagnetic directions of primary magnetizations could be compared with those from the Chiba section (Haneda et al. 2020). The correlation with the Chiba section based on relative paleointensity provides an age model with sedimentation rates of 30 cm/kyr and 18 cm/kr for the intervals above and below the Byk-E tephra. The age for the main directional swing from reversed to normal polarities could be estimated as 772.8 ± 0.5 ka, which is consistent with the age 772.9 ka reported for the Chiba section (Suganuma et al. 2018).

Abbreviations

AF: Alternating field; AFD: Alternating field demagnetization; AGM: Alternating gradient magnetometer; AIST: National Institute of Advanced Industrial Science and Technology; ARM: Anhysteretic remanent magnetization; Byk: Ontake-Byakubi; DC: Direct current; EDS: Energy dispersive X-ray spectroscopy; EBSD: Electron back-scattered diffraction; FORC: First order reversal curve; GSJ: Geological Survey of Japan; GSSP: Global Boundary Stratotype Section and Point; IRM: Isothermal remanent magnetization; LTD: Low-temperature demagnetization; M–B boundary: Matuyama–Brunhes boundary; MD: Multidomain; NIRE: National Institute for Rural Engineering; NRM: Natural remanent magnetization; PSD: Pseudo-single domain; SD: Single domain; SV: Single vortex; SEM: Scanning electron microscope; SQUID: Superconducting Quantum Interference Device; SRM: SQUID rock magnetometer; PAFD: Progressive alternating field demagnetization; PThD: Progressive thermal demagnetization; ThD: Thermal demagnetization; VSM: Vibrating sample magnetometer.

Supplementary Information

The online version contains supplementary material available at https://doi.org/10.1186/s40623-022-01626-1.

Additional file 1: Figure S1. (a) Map of Japanese Islands. Red open rectangle is the area shown in Figure S1b. (b) Simplified geological map of Mobara area, Boso Peninsula. The Kiwada, Otadai, Umegase, Kokumoto, Kakinokidai, Chonan, Kasamori and Kongochi Formations are shown in stratigraphic ascending order from southeast to northwest. Red solid rectangles are the localities, where Byk-E tephra layer is identified, including the Terasaki Shinden-Nishi site for this study. The M44, Chonan, and Chiba sections were studied by Nanayama et al. (2016), Okada and Nitsuma (1989), and Suganuma et al. (2021), respectively.

Additional file 2: Figure S2. (a) Schematic columnar section of Kazusa Group. Key tephras, magnetostratigraphy, biostratigraphy, marine isotope stages (MIS) stratigraphy, sequence stratigraphy, ages of tephras based on radiometric datings and correlations are shown. Base of Kazusa Group is suggested as 2.3 Ma based on tephrastratigraphy (Tamura et al., 2019). (b) Schematic lithology column of the Kokumoto Formation. Key tephras, magnetostratigraphy, and biostratigraphy are also shown. Red bar shows massive mudstone used for this study. Magnetozones in the magnetostratigraphy column in a are based on Niitsuma (1976). Geomagnetic

reversal ages of the boundaries of Chrons and Subchrons are based on Gradstein et al. (2020) except for Reunion Subchron. Ages for the upper and lower boundaries of Reunion Subchron are based on Simon et al. (2018).

Additional file 3: Figure S3. (a) Photo of thick sand bed underlying the studied silt layer (right hand side) along a roadside. The outcrop for paleomagnetic sampling is above and behind the bushes, which is not directly visible from this point. (b) Photo of a 3 mm thick tephra B; light colored fragmented horizontal layer shown by red arrows. (c) Photo of paleomagnetic sampling on an outcrop with an electrically powered diamond drill.

Additional file 4: Figure S4. Horizons of paleomagnetic samples on the outcrop for blocks A through G. Samples from blocks A through F were taken during the first sampling tour, and samples for block G was taken during the second sampling tour. Please note that not all the numbered drill cores were sampled due to broken connection of the bottom to the outcrop. The sampled drill cores are listed in Table S1a.

Additional file 5: Figure S5. Results of least squares fitting of lines and circles, and combined analyses of remagnetization circles using Paleomagnetism.org 2.0 (Koymans et al., 2020). (a) Sample 24 and (b) sample 89 are examples showing reversed and normal polarities, respectively. For each sample, one specimen is fitted with a great circle (top figure), and two specimens give line fitted directions (second and third figures from the top). Left figures are vector endpoint diagrams and right figures are equal-area projections. Red lines or curves on the diagrams are the results of least squares fitting with a line or a circle. Tables in the middle are the summary of linear and great circle fittings and combined analyses). Bottom figures are the results of combined analyses plotted on equal-area projections. Alphabets and numbers on the symbols of the vector endpoint diagrams are demagnetization methods (i.e. A=AFD, T=ThD, L=LTD) and demagnetization levels (for LTD, AFD levels prior to the application of LTD).

Additional file 6: Table S1a. List of samples used for paleomagnetic measurements and analyses. **S1b**. Summary of demagnetization methods.

Additional file 7: Table S2. Combined analysis of remagnetization great circles as well as linear regression lines.

Additional file 8: Table S3. Summary of relative paleointensity estimates.

Additional file 9: Table S4. Summary of volume magnetic susceptibility, kARM and Sratio.

Additional file 10. References for additional files.

Additional file 11. Data files of palgomagnetic results for Paleomagnetism.org 2.0.

Acknowledgements
The authors thank Ayako Katayama for performing the paleomagnetic and rock magnetic measurements and for producing the artworks. The authors are grateful to Emiko Miyamura for helping with paleomagnetic measurements and Tetsuro Sato for helping with the measurements with the AGM.

Author contributions
HO conducted sampling, designed experiments, and wrote most of the manuscript; FN conducted sampling and edited the manuscript; HN conducted sampling, analyzed and identified the volcanic ash layers, and edited the manuscript. YH conducted electron microscopy analyses of sediments, including EDS and EBSD, and edited manuscript. All the authors read and approved the final manuscript.

Funding
Hirokuni Oda was supported by JSPS KAKENHI Grant Numbers 19H00706, 20KK0082, and 21H04523.

Availability of data and materials
Data will be available upon request to the authors.

Declarations

Competing interests
The authors declare that they have no competing interests.

Author details
[1]Research Institute of Geology and Geoinformation, Geological Survey of Japan, AIST, Central 7, 1-1-1 Higashi, Tsukuba 305-8567, Japan. [2]Institute for Rural Engineering, NARO, 2-1-6 Kannondai, Tsukuba 305-8609, Japan.

Received: 11 October 2021 Accepted: 8 April 2022
Published online: 27 May 2022

References

Bloemendal J, King JW, Hall FR, Doh S-J (1992) Rock magnetism of late Neogene and Pleistocene deep-sea sediments: relationship to sediment source, diagenetic processes, and sediment lithology. J Geophys Res 97:4361–4375. https://doi.org/10.1029/91JB03068

Borchardt GA, Harward ME, Schmitt RA (1971) Correlation of volcanic ash deposits by activation analysis of glass separates. Quat Res 1:247–260. https://doi.org/10.1016/0033-5894(71)90045-7

Channell JET (2017) Complexity in Matuyama-Brunhes polarity transitions from North Atlantic IODP/ODP deep-sea sites. Earth Planet Sci Lett 467:43–56. https://doi.org/10.1016/j.epsl.2017.03.019

Channell JET, Kleiven HF (2000) Geomagnetic palaeointensities and astrochronological ages for the Matuyama-Brunhes boundary and the boundaries of the Jaramillo Subchron: Palaeomagnetic and oxygen isotope records from ODP Site 983. Philos Trans R Soc Lond, a: Math Phys Eng Sci 358:1027–1047. https://doi.org/10.1098/rsta.2000.0572

Channell JET, Hodell DA, Singer BS, Xuan C (2010) Reconciling astrochronological and 40Ar/39Ar ages for the Matuyama-Brunhes boundary and late Matuyama chron. Geochem Geophys Geosyst 11:Q0AA12. https://doi.org/10.1029/2010GC003203

Cherepanova MV, Pushkar VS, Razjigaeva N, Kumai H, Koizumi I (2002) Diatom biostratigraphy of the Kazusa Group, Boso Peninsula, Honshu, Japan. Quat Res (daiyonki Kenkyu) 41:1–10. https://doi.org/10.4116/jaqua.41.1

Clement BM (1991) Geographical distribution of transitional VGPs: evidence for non-zonal equatorial symmetry during the Matuyama–Brunhes geomagnetic reversal. Earth Planet Sci Lett 104:48–58. https://doi.org/10.1016/0012-821X(91)90236-B

Clement BM, Kent DV (1991) A Southern Hemisphere record of the Matuyama–Brunhes polarity reversal. Geophys Res Lett 18:81–84. https://doi.org/10.1029/90GL02714

Coe RS, Singer BS, Pringle MS, Zhao XX (2004) Matuyama–Brunhes reversal and Kamikatsura event on Maui: paleomagnetic directions, Ar-40/Ar-39 ages and implications. Earth Planet Sci Lett 222:667–684. https://doi.org/10.1016/j.epsl.2004.03.003

Day R, Fuller M, Schmidt VA (1977) Hysteresis properties of titanomagnetites: grain size and composition dependence. Phys Earth Planet Inter 13:260–267. https://doi.org/10.1016/0031-9201(77)90108-X

deMenocal PB, Ruddiman WF, Kent DV (1990) Depth of post-depositional remanence acquisition in deep-sea sediments—a case study of the Brunhes–Matuyama reversal and oxygen isotopic stage 19.1. Earth Planet Sci Lett 99:1–13. https://doi.org/10.1016/0012-821X(90)90066-7

Dreyfus GB, Raisbeck GM, Parrenin F, Jouzel J, Guyodo Y, Nomade S, Mazaud A (2008) An ice core perspective on the age of the Matuyama–Brunhes boundary. Earth Planet Sci Lett 274:151–156. https://doi.org/10.1016/j.epsl.2008.07.008

Dunlop DJ (2002) Theory and application of the Day plot (Mrs/Ms versus Hcr/Hc): 1. Theoretical curves and tests using titanomagnetite data. J Geophys Res: Solid Earth 107:2056. https://doi.org/10.1029/2001JB000486

Froggatt PC (1992) Standardization of the chemical analysis of tephra deposits. Report of the ICCT working group. Quat Inter 13(14):93–96. https://doi.org/10.1016/1040-6182(92)90014-S

Gu X, Heaney PJ, Aarão Reis FDA, Brantley SL (2020) Deep abiotic weathering of pyrite. Science 370:eabb8092. https://doi.org/10.1126/science.abb8092

Haneda Y, Okada M, Suganuama Y, Kitamura T (2020) A full sequence of the Matuyama–Brunhes geomagnetic reversal in the Chiba composite section, central Japan. Prog Earth Planet Sci 7:44. https://doi.org/10.1186/s40645-020-00354-y

Harrison RJ, Feinberg JM (2008) FORCinel: An improved algorithm for calculating first-order reversal curve distributions using locally weighted regression smoothing. Geochem Geophys Geosyst 9:Q05016. https://doi.org/10.1029/2008GC001987

Harrison RJ, Muraszko J, Heslop D, Lascu I, Muxworthy AR, Roberts AP (2018) An improved algorithm for unmixing first-order reversal curve diagrams using principal component analysis. Geochem Geophys Geosyst 19:1595–1610. https://doi.org/10.1029/2018GC007511

Hoffman KA, Mochizuki N (2012) Evidence of a partitioned dynamo reversal process from paleomagnetic recordings in Tahitian lavas. Geophys Res Lett 39:L06303. https://doi.org/10.1029/2011GL050830

Hoffman KA, Camps P, Carlton M (2020) Rare palaeomagnetic evidence of long-term mantle control of the geodynamo and possible role of the NAD field in the reversal process. Geophys J Inter 221:142–150. https://doi.org/10.1093/gji/ggz480

Hyodo M, Katoh S, Kitamura A, Takasaki K, Matsushita H, Kitaba I, Tanaka I, Nara M, Matsuzaki T, Dettman DL, Okada M (2016) High resolution stratigraphy across the early-middle Pleistocene boundary from a core of the Kokumoto formation at Tabuchi, Chiba Prefecture, Japan. Quat Int 397:16–26. https://doi.org/10.1016/j.quaint.2015.03.031

Ito M (1992) High-frequency depositional sequences of the upper part of the Kazusa Group, a middle Pleistocene forearc basin fill in Boso Peninsula, Japan. Sed Geol 76:155–175. https://doi.org/10.1016/0037-0738(92)90081-2

Ito H, Nanayama F, Nakazato H (2017) Zircon U-Pb dating using LA-ICP-MS: Quaternary tephras in Boso Peninsula, Japan. Quat Geochronol 40:12–22. https://doi.org/10.1016/j.quageo.2016.07.002

Ito M, Kameo M, Satoguchi Y, Masuda F, Hiroki Y, Takano O, Nakajima T, Suzuki N (2016) Neogene-Quaternary sedimentary successions. In: Moreno T, Wallis S, Kojima T, Gibbons W (eds) The geology of Japan. Geological Society of London, London, pp 309–337. https://doi.org/10.1144/GOJ.12

Kasuya M (1990) Fission-track ages of tuff layers related to the Plio-Pleistocene boundary on the Boso Peninsula, Japan. Quat Res 33:86–93. https://doi.org/10.1016/0033-5894(90)90086-Z

Kazaoka O, Suganuma Y, Okada M, Kameo K, Head MJ, Yoshida T, Sugaya M, Kameyama S, Ogitsu I, Nirei H, Aida N, Kumai H (2015) Stratigraphy of the Kazusa Group, Chiba Peninsula, Central Japan: an expanded and highly-resolved marine sedimentary record from the Lower and Middle Pleistocene. Quat Int 383:116–134. https://doi.org/10.1016/j.quaint.2015.02.065

Kirschvink J (1980) The least-squares line and plane and the analysis of palaeomagnetic data. Geophys J Roy Astr S 62:699–718. https://doi.org/10.1111/j.1365-246X.1980.tb02601.x

Koch CB, Oxborrow CA, Morup S, Madsen MB, Quinn AJ, Coey JMD (1995) Magnetic properties of feroxyhyte (δ-FeOOH). Phys Chem Minerals 22:333–341. https://doi.org/10.1007/BF00202774

Koymans MR, Langereis CG, Pastor-Galán D, van Hinsbergen DJJ (2016) Paleomagnetism.org: An online multi-platform open source environment for paleomagnetic data analysis. Comput Geosci 93:127–137. https://doi.org/10.1016/j.cageo.2016.05.007

Koymans MR, van Hinsbergen DJ, Pastor-Galán D, Vaes B, Langereis CG (2020) Towards FAIR paleomagnetic data management through Paleomagnetism.org 2.0. Geochem Geophys Geosyst 21:e2019GC008838. https://doi.org/10.1029/2019GC008838

Kuiper KF, Deino A, Hilgen FJ, Krijgsman W, Renne PR, Wijbrans JR (2008) Synchronizing rock clocks of earth history. Science 320:500–504. https://doi.org/10.1126/science.1154339

Laj C, Mazaud A, Weeks R, Fuller M, Herrero-Bervera E (1991) Geomagnetic reversal paths. Nature 351:447. https://doi.org/10.1038/351447a0

Lascu I, Harrison RJ, Li Y, Muraszko JR, Channell JET, Piotrowski AM, Hodell DA (2015) Magnetic unmixing of first-order reversal curve diagrams using principal component analysis. Geochem Geophys Geosyst 16:2900–2915. https://doi.org/10.1002/2015GC005909

Leonhardt R, Fabian K (2007) Paleomagnetic reconstruction of the global geomagnetic field evolution during the Matuyama/Brunhes transition: Iterative Bayesian inversion and independent verification. Earth Planet Sci Lett 253:172–195. https://doi.org/10.1016/j.epsl.2006.10.025

Lowrie W (1990) Identification of ferromagnetic minerals in a rock by coercivity and unblocking temperature properties. Geophys Res Lett 17:159–162. https://doi.org/10.1029/GL017I002P00159

Machida H, Arai F, Sugihara S (1980) Tephrochronological study on the middle Pleistocene deposits in the Kanto and Kinki districts, Japan. Quat Res (daiyonki Kenkyu) 19:233e261. https://doi.org/10.4116/jaqua.19.233 **(in Japanese with English abstract)**

McFadden PL, McElhinny MW (1988) The combined analysis of remagnetisation circles and direct observations in paleomagnetism. Earth Planet Sci Lett 87:161–172. https://doi.org/10.1016/0012-821X(88)90072-6

Merrill RT, McFadden PL (1999) Geomagnetic polarity transitions. Rev Geophys 37:201–226. https://doi.org/10.1029/1998RG900004

Mochizuki N, Oda H, Ishizuka O, Yamazaki T, Tsunakawa H (2011) Paleointensity variation across the Matuyama-Brunhes polarity transition: observations from lavas at Punaruu Valley, Tahiti. J Geophys Res: Solid Earth 116:B06103. https://doi.org/10.1029/2010JB008093

Morin FJ (1950) Magnetic susceptibility of α-Fe2O3 and α-Fe2O3 with added titanium. Phys Rev 78:819–820. https://doi.org/10.1103/PhysRev.78.819.2

Nakagawa T (2020) A coupled core-mantle evolution: review and future prospects. Prog Earth Planet Sci 7:57. https://doi.org/10.1186/s40645-020-00374-8

Nakagawa H, Niitsuma N, Hayasaka I (1969) Late Cenozoic geomagnetic chronology on the Boso Peninsula. J Geol Soc Jpn 73:267–281. https://doi.org/10.5575/geosoc.75.267 **(in Japanese, with English abstract)**

Nanayama F, Nakazato H, Ooi S, Nakashima R, (2016) Geology of the Mobara District. Quadrangle Series, 1:50,000. Geological Survey of Japan, AIST, 101. (in Japanese with English abstract)

Niitsuma N (1971) Detailed study of the sediments recording the Matuyama–Brunhes geomagnetic reversal. Sci Rep Tohoku Univ 2nd Ser (geol) 43:1–39

Niitsuma N (1976) Magnetic stratigraphy in the Boso peninsula. J Geol Soc Jpn 82:163–181. https://doi.org/10.5575/geosoc.82.163 **(in Japanese with English abstract)**

Nishida N, Kazaoka O, Izumi K, Suganuma Y, Okada M, Yoshida T, Ogitsu I, Nakazato H, Kameyama S, Kagawa A, Morisaki M, Nirei N (2016) Sedimentary processes and depositional environments of a continuous marine succession across the Lower-Middle Pleistocene boundary: Kokumoto Formation, Kazusa Group, central Japan. Quat Int 397:3–15. https://doi.org/10.1016/j.quaint.2015.06.045

Oda H, Shibuya H, Hsu V (2000) Palaeomagnetic records of the Brunhes/Matuyama polarity transition from ODP Leg 124 (Celebes and Sulu seas). Geophys J Int 142:319–338. https://doi.org/10.1046/j.1365-246x.2000.00130.x

Oda M (1977) Planktonic foraminiferal biostratigraphy of the late Cenozoic sedimentary sequence Central Honshu Japan. Sci Rep Tohoku Univ 2nd Ser Geol 48:1–76

Okada M, Niitsuma N (1989) Detailed paleomagnetic records during the Brunhes–Matuyama geomagnetic reversal, and a direct determination of depth lag for magnetization in marine sediments. Phys Earth Planet Inter 56:133–150. https://doi.org/10.1016/0031-9201(89)90043-5

Okada M, Suganuma Y, Haneda Y, Kazaoka O (2017) Paleomagnetic direction and paleointensity variations during the Matuyama–Brunhes polarity transition from a marine succession in the Chiba composite section of the Boso Peninsula, central Japan. Earth Planets Space 69:45. https://doi.org/10.1186/s40623-017-0627-1

Ozdemir O, Dunlop DJ (1996) Thermoremanence and Neel temperature of goethite. Geophys Res Lett 23:921–924. https://doi.org/10.1029/96GL00904

Ozdemir O, Dunlop DJ, Moskowitz BM (1993) The effect of oxidation on the Verwey transition in magnetite. Geophys Res Lett 20:1671–1674. https://doi.org/10.1029/93GL01483

Ozima M, Ozima M, Akimoto S (1964) Low temperature characteristics of remanent magnetization of magnetite—Self-reversal and recovery phenomena of remanent magnetization. J Geomag Geoelectr 16:165–177. https://doi.org/10.5636/jgg.16.165

Pickering KT, Souter C, Oba T, Taira A, Schaaf M, Platzman E (1999) Glacioeustatic control on deep-marine clastic forearc sedimentation, Pliocene–mid-Pleistocene (c. 1180–600 ka) Kazusa Group, SE Japan. J Geol Soc Lond 156:125–136. https://doi.org/10.1144/gsjgs.156.1.0125

Raisbeck GM, Yiou F, Cattani O, Jouzel J (2006) ^{10}Be evidence for the Matuyama Brunhes geomagnetic reversal in the EPICA Dome C ice core. Nature 443:82–84. https://doi.org/10.1038/nature05266

Renne PR, Balco G, Ludwig KR, Mundil R, Min K et al (2011) Response to the comment by W.H. Schwarz et al. on "Joint determination of 40 K decay constants and 40Ar*/40 K for the Fish Canyon sanidine standard, and improved accuracy for 40Ar/39Ar geochronology" by P.R. Renne et al. (2010). Geochim Cosmochim Acta 75:5097–5100. https://doi.org/10.1016/j.gca.2011.06.021

Ricci J, Carlut J, Marques FO, Hildenbrand A, Valet J-P (2020) Volcanic record of the last geomagnetic reversal in a lava flow sequence from the Azores. Front Earth Sci 8:165. https://doi.org/10.3389/feart.2020.00165

Roberts AP, Taux L, Heslop D (2013) Magnetic paleointensity stratigraphy and high-resolution quaternary geochronology: successes and future challenges. Quat Sci Rev 61:1–16. https://doi.org/10.1016/j.quascirev.2012.10.036

Roberts AP, Heslop D, Zhao X, Pike CR (2014) Understanding fine magnetic particle systems through use of first-order reversal curve diagrams. Rev Geophys 52:557–602. https://doi.org/10.1002/2014RG000462

Roberts AP, Tauxe L, Heslop D, Zhao X, Jiang Z (2018a) A critical appraisal of the "Day" diagram. J Geophys Res: Solid Earth 123:2618–2644. https://doi.org/10.1002/2017JB015247

Roberts AP, Zhao X, Harrison RJ, Heslop D, Muxworthy AR, Rowan CJ, Larrasoaña J-C, Florindo F (2018b) Signatures of reductive magnetic mineral diagenesis from unmixing of first-order reversal curves. J Geophys Res: Solid Earth 123:4500–4522. https://doi.org/10.1029/2018JB015706

Roberts AP, Chang L, Rowan CJ, Horng C-S, Florindo F (2011) Magnetic properties of sedimentary greigite (Fe_3S_4): an update. Rev Geophys 49:RG1002. https://doi.org/10.1029/2010RG000336

Sato M, Terada T, Mochizuki N, Tsunakawa H (2019) Experimental evaluation of remanence carriers using the microcoercivity-unblocking temperature diagram. Geochem Geophys Geosyst 20:5177–5191. https://doi.org/10.1029/2019GC008534

Sato T, Takayama T, Kato M, Kudo T, Kameo K (1988) Calcareous microfossil biostratigraphy of the uppermost Cenozoic formations distributed in the coast of the Japan Sea, part 4: conclusion. J Jpn Assoc Pet Technol 53:474–491. https://doi.org/10.3720/JAPT.53.9 **(in Japanese with English abstract)**

Satoguchi Y, Nagahashi Y (2012) Tephrostratigraphy of the Pliocene to middle Pleistocene series in Honshu and Kyushu islands, Japan. Island Arc 21:149–169. https://doi.org/10.1111/j.1440-1738.2012.00816.x

Shackleton NJ, Berger A, Peltier WR (1990) An alternative astronomical calibration of the Lower Pleistocene timescale based on ODP Site 677. Trans R Soc Edinb Earth Sci 81:251–261. https://doi.org/10.1017/S0263593300020782

Simon Q, Thouveny N, Bourlès DL, Valet JP, Bassinot F, Ménabréaz L, Guillou V, Choy S, Beaufort L (2016) Authigenic ^{10}Be/^{9}Be ratio signatures of the cosmogenic nuclide production linked to geomagnetic dipole moment variation since the Brunhes/Matuyama boundary. J Geophys Res Solid Earth 121:7716–7741. https://doi.org/10.1002/2016JB013335

Simon Q, Thouveny N, Bourlès DL, Bassinot F, Savranskaia T, Valet JP (2018) Increased production of cosmogenic ^{10}Be recorded in oceanic sediment sequences: information on the age, duration, and amplitude of the geomagnetic dipole moment minimum over the Matuyama–Brunhes transition. Earth Planet Sci Lett 489:191–202. https://doi.org/10.1016/j.epsl.2018.02.036

Simon Q, Suganuma Y, Okada M, Haneda Y, ASTER team, (2019) High-resolution ^{10}Be and paleomagnetic recording of the last polarity reversal in the Chiba composite section: Age and dynamics of the Matuyama–Brunhes transition. Earth Planet Sci Lett 519:92–100. https://doi.org/10.1016/j.epsl.2019.05.004

Singer BS, Hoffman KA, Coe RS, Brown LL, Jicha BR, Pringle MS, Chauvin A (2005) Structural and temporal requirements for geomagnetic field reversal deduced from lava flows. Nature 434:633–636. https://doi.org/10.1038/nature03431

Suganuma Y, Yokoyama Y, Yamazaki T, Kawamura K, Horng CS, Matsuzaki H (2010) ^{10}Be evidence for delayed acquisition of remanent magnetization in marine sediments: implication for a new age for the Matuyama–Brunhes boundary. Earth Planet Sci Lett 296:443–450. https://doi.org/10.1016/j.epsl.2010.05.031

Suganuma Y, Okuno J, Heslop D, Roberts AP, Yamazaki T, Yokoyama Y (2011) Post-depositional remanent magnetization lock-in for marine sediments deduced from ^{10}Be and paleomagnetic records through the Matuyama–Brunhes boundary. Earth Planet Sci Lett 311:39–52. https://doi.org/10.1016/j.epsl.2011.08.038

Suganuma Y, Okada M, Horie K, Kaiden H, Takehara M, Senda R, Kimura J, Kawamura K, Haneda Y, Kazaoka O, Head MJ (2015) Age of Matuyama–Brunhes boundary constrained by U-Pb zircon dating of a widespread tephra. Geology 43:491–494. https://doi.org/10.1130/G36625.1

Suganuma Y, Haneda Y, Kameo K, Kubota Y, Hayashi H, Itaki T, Okuda M, Head MJ, Sugaya M, Nakazato H, Igarashi A, Shikoku K, Hongo M, Watanabe M, Satoguchi Y, Takeshita Y, Nishida N, Izumi K, Kawamura K, Kawamata M, Okuno J, Yoshida T, Ogitsu I, Yabusaki H, Okada M (2018) Paleoclimatic and paleoceanographic records through Marine Isotope Stage 19 at the Chiba composite section, central Japan: a key reference for the Early-Middle Pleistocene Subseries boundary. Quat Sci Rev 191:406–430. https://doi.org/10.1016/j.quascirev.2018.04.022

Suganuma Y, Okada M, Head MJ, Kameo K, Haneda Y, Hayashi H, Irizuki T, Itaki T, Izumi K, Kubota Y, Nakazato H, Nishida N, Okuda M, Satoguchi Y, Simon Q, Takeshita Y (2021) Formal ratification of the Global Boundary Stratotype Section and Point (GSSP) for the Chibanian Stage and Middle Pleistocene Subseries of the Quaternary System: the Chiba Section, Japan. Episodes 44:317–347. https://doi.org/10.18814/epiiugs/2020/020080

Suzuki T, Fujiwara O, Danhara T (1998) Fission track ages of several Quaternary tephras in Kanto and Chubu regions, Central Japan. J Geopgrahy 107:348–367. https://doi.org/10.5026/JGEOGRAPHY.107.3_348 **(in Japanese with English abstract)**

Takeshita Y, Matsushima N, Teradaira H, Uchiyama T, Kumai H (2016) A marker tephra bed close to the Lower-Middle Pleistocene boundary: distribution of the Ontake-Byakubi Tephra Bed in central Japan. Quat Inter 397:27–38. https://doi.org/10.1016/j.quaint.2015.03.054

Tassin T, Gastine T, Fournier A (2021) Geomagnetic semblance and dipolar-multipolar transition in top-heavy double-diffusive geodynamo models. Geophys J Inter 226:1897–1919. https://doi.org/10.1093/gji/ggab161

Tokuhashi S, Danhara T, Endo H, Isoda K, Nishimura S (1983) Some experiments and problems on fission-track dating of geologically younger-age samples: with special reference to several volcanic ash layers in Kazusa and Shimosa Groups, Boso Peninsula, central Japan. Bull Geol Surv Jpn 34:241–269 **(in Japanese)**

Torii M, Fukuma K, Horng C-S, Lee T-Q (1996) Magnetic discrimination of pyrrhotite- and greigite-bearing sediment samples. Geophys Res Lett 23:1813–1816. https://doi.org/10.1029/96GL01626

Tsuji T, Miyata Y, Okada M, Mita I, Nakagawa H, Sato Y, Nakamizu M (2005) High resolution chronology of the lower Pleistocene Otadai and Umegase Formations of the Kazusa Group, Boso Peninsula, central Japan: chronostratigraphy of the JNOC TR-3 cores based on oxygen isotope, magnetostratigraphy and calcareous nannofossil. J Geol Soc Jpn 111:1–20. https://doi.org/10.5575/geosoc.111.1 **(in Japanese with English abstract)**

Tsunakawa H, Okada M, Niitsuma N (1995) About 100 year directional variations in the Matuyama-Brunhes transition field inferred from the sedimentary records in the Boso Peninsula, Japan. J Geomag Geoelectr 47:337–345. https://doi.org/10.5636/jgg.47.337

Tsunakawa H, Okada M, Niitsuma N (1999) Further application of the deconvolution method of post-depositional DRM to the precise record of the Matuyama–Brunhes reversal in the sediments from the Boso Peninsula, Japan. Earth Planet Space 51:169–173. https://doi.org/10.1186/BF03352221

Valdez-Grijalva MA, Nagy L, Muxworthy AR, Williams W, Roberts AP, Heslop D (2020) Micromagnetic simulations of first-order reversal curve (FORC) diagrams of framboidal greigite. Geophys J Inter 222:1126–1134. https://doi.org/10.1093/gji/ggaa241

Valet JP, Fournier A (2016) Deciphering records of geomagnetic reversals. Rev Geophys. https://doi.org/10.1002/2015RG000506

Valet JP, Meynadier L, Guyodo Y (2005) Geomagnetic dipole strength and reversal rate over the past two million years. Nature 435:802–805. https://doi.org/10.1038/nature03674

Valet JP, Bassinot F, Bouilloux A, Bourlès D, Nomade S, Guillou V, Lopes F, Thouveny N, Dewilde F (2014) Geomagnetic, cosmogenic and climatic changes across the last geomagnetic reversal from Equatorial Indian Ocean sediments. Earth Planet Sci Lett 397:67–79. https://doi.org/10.1016/j.epsl.2014.03.053

Valet JP, Bassinot F, Simon Q, Savranskaia T, Thouveny N, Bourlés DL, Villedieu A (2019) Constraining the age of the last geomagnetic reversal from geochemical and magnetic analyses of Atlantic, Indian, and Pacific Ocean sediments. Earth Planet Sci Lett 506:323–331. https://doi.org/10.1016/j.epsl.2018.11.012

Van Velzen A, Zijderveld J (1992) A method to study alterations of magnetic minerals during thermal demagnetization applied to a fine-grained marine marl (Trubi formation, Sicily). Geophys J Int 110:79–90. https://doi.org/10.1111/j.1365-246X.1992.tb00715.x

Verwey EJW (1939) Electronic conduction of magnetite (Fe_3O_4) and its transition point at low temperatures. Nature 144:327–328. https://doi.org/10.1038/144327b0

Watanabe M, Danhara T (1996) Fission track ages of volcanic ash layers of the Kazusa Group in the Boso Peninsula, central Japan. J Geol Soc Jpn 102:545–556. https://doi.org/10.5575/geosoc.102.545

Publisher's Note